# Discrete Modelling of Deterministic Size Effect of Normal-strength and Ultra-high Performance Concrete under Compression

**By**

**Lin Wan-Wendner [1], Giovanni Di Luzio* [2]**

A Paper submitted to

Construction and Building Materials

March 29, 2022

Corresponding Author

*Giovanni Di Luzio

Associate Professor

Department of Civil and Environmental Engineering

Politecnico di Milano

Piazza Leonardo da Vinci n. 32

20133 Milano, Italy

Tel.: +39 02 2399 4278

Fax: +39 02 2399 4220

[1]Research Associate, Department of Civil and Environmental Engineering, Politecnico di Milano, Email: lin.wan@u.northwestern.edu

[2]*Corresponding Author, Associate Professor, Department of Civil and Environmental Engineering, Politecnico di Milano, Email: giovanni.diluzio@polimi.it

**Abstract**

Size effect of heterogeneous granular materials under tensile loading is a well known phenomenon and the subsequent size effect laws are widely available in the scientific literature. On the contrary, size effect in compression is scarcely studied, which, especially for concrete, is more significant for its brittle failure mode in practical applications. This paper investigates the deterministic size effect in compression of concretes including a normal strength concrete (NSC) and an ultra high performance concrete (UHPC). The Lattice Discrete Particle Model (LDPM) is selected to determine the compressive strength of a broad range of sizes utilizing experimental-based calibrated data sets. The simulated tests include both cylinders and prisms with the diameter/width range from 150 mm to 600 mm for normal strength concrete and from 50 mm to 200 mm for UHPC. The investigated aspect ratio ranges from 1 to 16. It is found that the simulated strength show no size effect under low friction loading, and the magnitude of size effect decreases with rising aspect ratio under high friction loading. The size effect laws available in the literature are typically investigated by fitting the compressive strength data and found with limitations. A new compressive size effect law formula named ComSEL3D is proposed in terms of diameter and aspect ratio. The correlation by ComSEL3D for the simulated strengths is above 0.99, which shows its excellent ability in describing and predicting the deterministic size effect behavior in compression for both concretes in cylindrical and prism shapes. The ComSEL3D also outperforms the available formulas in the literature in matching the experimental results of various concretes under compression.

keywords: Concrete Failure, Size Effect, Compression, UHPC, CSEL, ComSEL

## 1 Introduction

Concrete is the most commonly used construction material on earth, employed extensively in buildings, bridges, roads and dams. Researchers around the world in the field of civil engineering conduct numerous laboratory tests each day to evaluate the strength capacity of different types of concrete. Thanks to the size effect laws [2, 3], the strengths of a structural scale concrete member can be estimated based on the smaller-scale laboratory test results with enough safety margin. For example, the energy-based size effect law (SEL) of Bažant has been recently incorporated into the ACI design code articles for beam shear and slab punching, see ACI-318/2019 [5].

In the last decades many researchers have intensively studied the size effect of concrete, but most

of these investigations were focused on tensile or indirect-tensile loading, see among many others [7–11]. In addition to the well-known size effect in tension, the size effect in compression has also been clearly demonstrated [2, 4, 13, 14] for concrete (for a review see [15]). Early work on the size effect in compression dates back to almost one century ago [14] in which the influence of age, cement/water ratio, and maximum aggregate size on the compressive strength were studied, concluding that the cylindrical specimen 6 x 12 inch (15.24 x 30.48 cm) provides a satisfactory shape and dimension in order to obtain consistent results. Later experimental investigations were also performed under uniaxial loading in [6, 13, 16–18]. Other experiments were executed under small eccentric compression uniaxial load on microconcrete [19], plain concrete columns [20, 21], reinforced concrete columns [22], sandstone specimens and plain concrete cylinders [23].

However, the size dependence of compressive strength of concrete is not yet fully studied nor understood. Although the mechanisms of concrete size effect in compression are really complex to be fully identified, size effect is very important in terms of structural and material design because its presence must be expected when concrete fails in compression, e.g., failure in bending of prestressed concrete or over-reinforced concrete beams. The experimental investigation of the concrete size effect comes with two main disadvantages. Firstly, the size of the specimens that can be tested in laboratories is limited due to restricted space, testing machine boundaries and loading capacity, and weight of the samples. Secondly, the test results can be easily influenced by machine compliance, test setup, specimen and machine preparation, and uncertainty factors from human testers. This might lead to incomplete inaccurate data set, missing sizes, and large scatter in testing results. Thus, a reliable computational tool, capable of describing and predicting the mechanical behavior of concrete materials, is a more suitable alternative to investigate the concrete size effect. This option is explored in the present study.

The Lattice Discrete Particle Model (LDPM) [40, 41] is selected to determine the material compressive strength of a broad range of sizes utilizing experimental-based calibrated data sets. The deterministic size effect in compression of two types of concrete, a normal strength concrete (NSC) and an ultra-high performance concrete (UHPC), is investigated in this research. The mesoscale discrete model, LDPM, is chosen because concrete is a composite material with a complex and random internal structure (aggregates, matrix, interphases, and pores) and its mesostructure strongly affects the macroscopic mechanical

behavior under loading. Microcracks precede the formation of larger cracks that coalesce within the failure zone/zones and these cracks or slip mechanisms are discontinuities in the displacement field at different scales of observation. Modeling the localization of distributed microcracking into a finite-size fracture process zone, and the resulting quasi-brittle behavior of the material volume, is essential to many applications, such as in compressive failure. In addition, the heterogeneous nature of these materials leads to a characteristic internal length that needs to be returned by the numerical model [2, 25]. Therefore, it is relatively difficult to incorporate such features into such models that assume continuity of the displacement field, though a few capable models exist, e.g. [26], see also [27] for a review. Alternatively, continuum-based models can account for crack kinematics by incorporating different kinds of discontinuities, see among others [28–30]. In contrast, the complex cracking mechanisms and failure can be effectively simulated using mesoscale discrete models, in which the material heterogeneity is automatically reproduced and the discontinuity that appears at the particle boundaries provides a natural way to represent cracks. For this reason, LDPM, which gives a more realistic representation of the cracking initiation and propagation for its discrete nature and considers the actual aggregate size distribution, was adopted in this study. LDPM has been proven to have excellent abilities simulating the mechanical behavior of various concrete materials, including regular concrete [40, 41], UHPC [42–44, 46], sulfur concrete [45], or different type of failure under uniaxial compression, triaxial compression, direct tension, tensile splitting, bending, shear with prestress [49], with fastening systems [47] as well as aging [42, 48] and size effect of concrete failed in compression and by tensile fracture [50].

Finally, the size effect laws available in the literature are used to fit the compressive strength data and are found with limitations on the size range and insufficient correlation. A new compressive size effect law formula named ComSEL3D is proposed in this paper, which has excellent ability in describing and predicting the size effect behavior in compression for both concretes and in different specimen shapes considered in this study.

## 2 Numerical model

In 2011, building on previous work [37–39], Cusatis and coworkers [40, 41] developed LDPM, a mesoscale discrete model that simulates the mechanical interaction of coarse aggregate pieces embedded in a binding

matrix. The geometrical representation of concrete mesostructure is constructed by randomly introducing and distributing spherical shaped coarse aggregate pieces inside the volume of interest and zero-radius aggregate pieces on the surface. Based on the Delaunay tetrahedralization of the generated particle centers, a three-dimensional domain tessellation creates a system of polyhedral cells (see Fig. 1) interacting through triangular facets and a corresponding lattice system. The full description of LDPM geometry is reported in Cusatis. et. al. [40, 41].

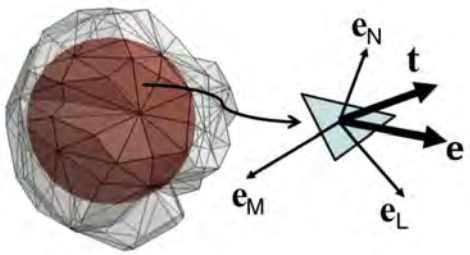


Figure 1: One LDPM Cell around an aggregate piece.

In LDPM, rigid body kinematics is used to describe the deformation of the lattice particle system and the displacement jump, $[\![\mathbf{u}_C]\!]$, at the centroid of each facet is used to define measures of strain as

$$e_N = \frac{\mathbf{n}^{\mathrm{T}}[\![\mathbf{u}_C]\!]}{\ell}; \quad e_L = \frac{\mathbf{l}^{\mathrm{T}}[\![\mathbf{u}_C]\!]}{\ell}; \quad e_M = \frac{\mathbf{m}^{\mathrm{T}}[\![\mathbf{u}_C]\!]}{\ell} \tag{1}$$

where $\ell$ = is the interparticle distance; and $\mathbf{n}$, $\mathbf{l}$, and $\mathbf{m}$, are unit vectors defining a local system of reference attached to each facet. A vectorial constitutive law governing the material behavior is imposed at the centroid of each facet. In the elastic regime, the normal and shear stresses are proportional to the corresponding strains: $t_N = E_N e_N^* = E_N(e_N - e_N^0)$; $t_M = E_T e_M^* = E_T(e_M - e_M^0)$; $t_L = E_T e_L^* = E_T(e_L - e_L^0)$, where $E_N = E_0$, $E_T = \alpha E_0$, $E_0$ = effective normal modulus, and $\alpha$ = shear-normal coupling parameter; and $e_N^0$, $e_M^0$, $e_L^0$ are mesoscale eigenstrains (if any present). For stresses and strains beyond the elastic limit, the LDPM formulation considers the following nonlinear mesoscale phenomena [37, 38, 40]: (1) fracture and cohesion; (2) compaction and pore collapse; and (3) internal friction.

**Fracture and cohesion due to tension and tension-shear.** For tensile loading ($e_N^* > 0$), the fracturing behavior is formulated through effective strain, $e^* = \sqrt{e_N^{*2} + \alpha(e_M^{*2} + e_L^{*2})}$, and stress, $t = \sqrt{t_N^2 + (t_M^2 + t_L^2)/\alpha}$, which define the normal and shear stresses as $t_N = e_N^*(t/e^*)$; $t_M = \alpha e_M^*(t/e^*)$; $t_L = \alpha e_L^*(t/e^*)$. The effective stress $t$ is incrementally elastic ($\dot{t} = E_0\dot{e}$) and must satisfy the inequal-

ity $0 \leq t \leq \sigma_{bt}(e,\omega)$ where $\sigma_{bt} = \sigma_0(\omega)\exp\left[-H_0(\omega)\langle e - e_0(\omega)\rangle/\sigma_0(\omega)\right]$, $\langle x\rangle = \max\{x,0\}$, and $\tan(\omega) = e_N^*/\sqrt{\alpha}e_T^* = t_N\sqrt{\alpha}/t_T$, and $e_T^* = \sqrt{e_M^{*2} + e_L^{*2}}$. The post peak softening modulus is defined as $H_0(\omega) = H_t(2\omega/\pi)^{n_t}$, where $H_t$ is the softening modulus in pure tension ($\omega = \pi/2$). LDPM provides a smooth transition between pure tension and pure shear ($\omega = 0$) with parabolic variation for strength given by $\sigma_0(\omega) = \sigma_t r_{st}^2\Big(-\sin(\omega) + \sqrt{\sin^2(\omega) + 4\alpha\cos^2(\omega)/r_{st}^2}\Big)/[2\alpha\cos^2(\omega)]$, where $r_{st} = \sigma_s/\sigma_t$ is the ratio of shear strength to tensile strength.

**Compaction and pore collapse from compression.** Normal stresses for compressive loading ($e_N^* < 0$) must satisfy the inequality $-\sigma_{bc}(e_D, e_V) \leq t_N \leq 0$, where $\sigma_{bc}$ is a strain-dependent boundary depending on the volumetric strain, $e_V$, and the deviatoric strain, $e_D = e_N - e_V$. The volumetric strain is computed by the volume variation of the Delaunay tetrahedra as $e_V = \Delta V/3V_0$ and is assumed to be the same for all facets belonging to a given tetrahedron. Beyond the elastic limit, $-\sigma_{bc}$ models pore collapse as a linear evolution of stress for increasing volumetric strain with stiffness $H_c$ for $-e_V \leq e_{c1} = \kappa_{c0}e_{c0}$: $\sigma_{bc} = \sigma_{c0} + \langle -e_V - e_{c0}\rangle H_c(r_{DV})$; $H_c(r_{DV}) = H_{c0}/(1 + \kappa_{c2}\langle r_{DV} - \kappa_{c1}\rangle)$; $\sigma_{c0}$ is the mesoscale compressive yield stress; $r_{DV} = e_D/e_V$ and $\kappa_{c1}$, $\kappa_{c2}$ are material parameters. Compaction and rehardening occur beyond pore collapse ($-e_V \geq e_{c1}$). In this case one has $\sigma_{bc} = \sigma_{c1}(r_{DV})\exp\left[(-e_V - e_{c1})H_c(r_{DV})/\sigma_{c1}(r_{DV})\right]$ and $\sigma_{c1}(r_{DV}) = \sigma_{c0} + (e_{c1} - e_{c0})H_c(r_{DV})$.

**Friction due to compression-shear.** For compression dominated loading conditions ($e_N^* < 0$), the incremental shear stresses are computed as $\dot{t}_M = E_T(\dot{e}_M^* - \dot{e}_M^{*p})$ and $\dot{t}_L = E_T(\dot{e}_L^* - \dot{e}_L^{*p})$, where $\dot{e}_M^{*p} = \dot{\xi}\partial\varphi/\partial t_M$, $\dot{e}_L^{*p} = \dot{\xi}\partial\varphi/\partial t_L$, and $\xi$ is the plastic multiplier with loading-unloading conditions $\varphi\dot{\xi} \leq 0$ and $\dot{\xi} \geq 0$. The plastic potential is defined as $\varphi = \sqrt{t_M^2 + t_L^2} - \sigma_{bs}(t_N)$, where the nonlinear frictional law for the shear strength is assumed to be $\sigma_{bs} = \sigma_s + (\mu_0 - \mu_\infty)\sigma_{N0}[1 - \exp(t_N/\sigma_{N0})] - \mu_\infty t_N$; $\sigma_{N0}$ is the transitional normal stress; $\mu_0$ and $\mu_\infty$ are the initial and final internal friction coefficients.

The compatibility and constitutive equations discussed above are completed through the equilibrium equations of each individual particle to arrive at the complete set of governing equations of the LDPM framework.

The aforementioned LDPM mesoscale parameters govern the facet constitutive law with their effect on the macroscopic model response. The normal elastic modulus and shear-normal coupling parameter govern LDPM response in the elastic regime. The mesoscale tensile strength and characteristic length, or

equivalently the tensile fracture energy, govern the softening tensile fracturing behavior of LDPM facets and consequently also the macroscopic softening. The softening exponent governs the interaction between shear and tensile behavior during softening at the facet level and accordingly influences the level of ductility after failure. The mesoscale shear strength is the facet strength for pure shear and has effect mostly on the macroscopic behavior in unconfined and confined compression. Other LDPM parameters which affect the macroscopic behavior in compression include the yielding compressive stress, transitional strain ratio, initial internal friction coefficient, internal asymptotic friction coefficient and transitional stress. In the following, the calibration of those LDPM parameters is obtained through the best fitting of the complete loaddisplacement curves of experimental tests, if they are available, or through the best fitting of the maximum load reached in the experiment that is typically available.

Within the framework of LDPM, the modeling of NSC and UHPC both uses the mesoscale discrete model that simulates the mechanical interaction of coarse aggregate pieces embedded in a binding matrix. Just as in reality, one main difference between NSC and UHPC is the aggregate size, which leads to different compactness and strength. As explained in next sections, the actual aggregate size of NSC is used, and coarse graining technique is used for UHPC to save computational cost, see Fig. 2. Another difference between NSC and UHPC mix is the type of cement and supplementary cementitious materials (SCMs), which leads to a huge difference in the mortar matrix between the aggregates. Besides, the nonlinear constitutive laws formulated on the LDPM facets have to simulate the effects of the aggregate particles that are not considered in the construction of the mesoscale geometry, i.e. the particle with dimension smaller than the minimum size. All these differences are captured by the aforementioned linear and nonlinear formulations at the facets in LDPM with the meso-scale parameters. Thus the difference in modeling NSC and UHPC by LDPM is to consider the mesoscale heterogeneity corresponding to coarse aggregate size and distribution, and at the same time calibrate the meso-scale parameters to capture the effects of matrix and smaller aggregates, in order to match the behavior on the macroscale.

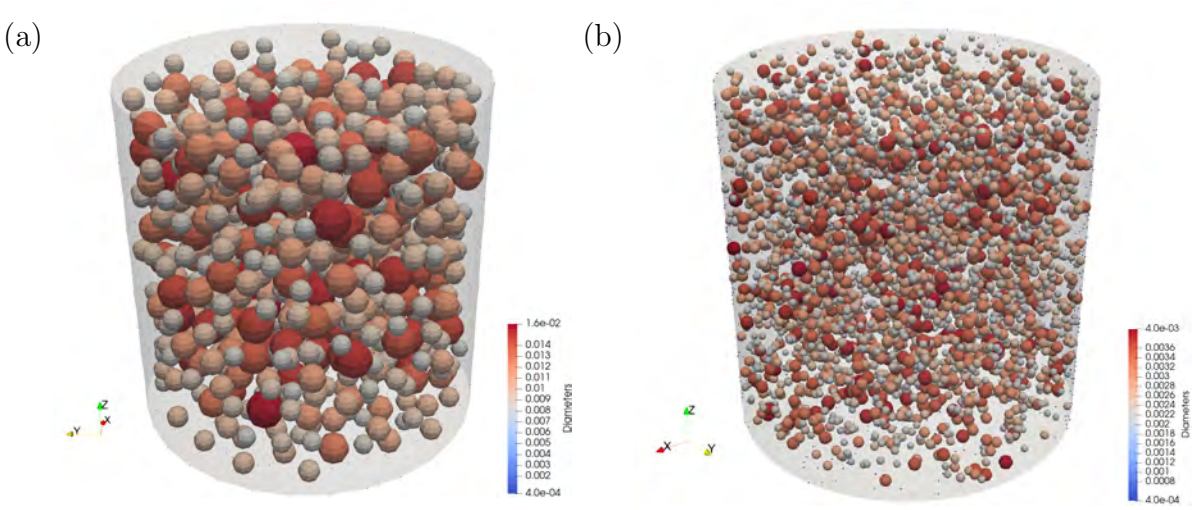


Figure 2: LDPM aggregate distribution for: (a) normal concrete cylinder 150x150mm and (b) UHPC cylinder 200x200 mm

### 2.1 LDPM Calibration for Normal Strength Concrete

The first concrete considered in this study has been experimentally characterized in [49, 51] and it is normal strength concrete with a target compressive strength of class C50/60, hereinafter abbreviated as C50. Its mixture constituents are listed in Table 1. Specimens, including cubes and prisms, for mechanical tests were cast by a computer aided mixing machine using wood and plastic molds. All formwork were removed 24 hours after casting. Then the specimens were stored at room temperature about 22°C and submerged in water until the day of mechanical tests.

Table 1: Constituents of Concrete C50/60 [49, 51]

| | | |
|---|---|---|
| Aggregate 0/4 mm edge | 101.85 | kg |
| Aggregate 0/4 mm round | 849.17 | kg |
| Aggregate 4/8 mm round | 370.79 | kg |
| Aggregate 8/16 mm round | 550.64 | kg |
| Water content | 181.00 | kg |
| Cement CEM 52.5 R | 464.90 | kg |
| Sky 657 | 6.67 | kg |
| w/c | 0.39 | - |

The experimental campaign includes unconfined compression, Young's modulus tests, prism splitting, and wedge splitting tests. The cubes have dimensions of 150×150×150 mm, while the prisms of 120×120×360 mm. The wedge splitting test (WST) setup can be found in Fig. 3. Cut from the cubes, the specimens for WST have dimensions as follows: width $w = 150$ mm, height $h = 130$ mm, thickness (not shown) t = 150 mm, the initial notch size a = 43 mm, the height of the crack ligament $h_{cr} = 100$ mm, and b = 50 mm (see Fig. ). Determined from the aforementioned experiments, the concrete C50 has unconfined compressive strength of about 82 MPa, Young's modulus of about 38 GPa and prism splitting strength of about 6 MPa averaged from tests carried out at 36 $\sim$ 56 days. The prism splitting stress and tensile strength is calculated as $\sigma = 2F/\pi Ld$, where $L$ is the length, $d$ is the depth/height of the specimen, and $F$ is the load or the maximum load, respectively. The testing results of cube compression, prism splitting and Young's modulus are listed in Table 2. When under wedge splitting test on 28 days of age, it reaches 12.2 kN of peak load. The authors are aware of the possible effects of the crack-parallel stress and its consequences in this type of tests [52] when the fracture energy is determined. However, the adopted numerical model is able to take into account that effect.

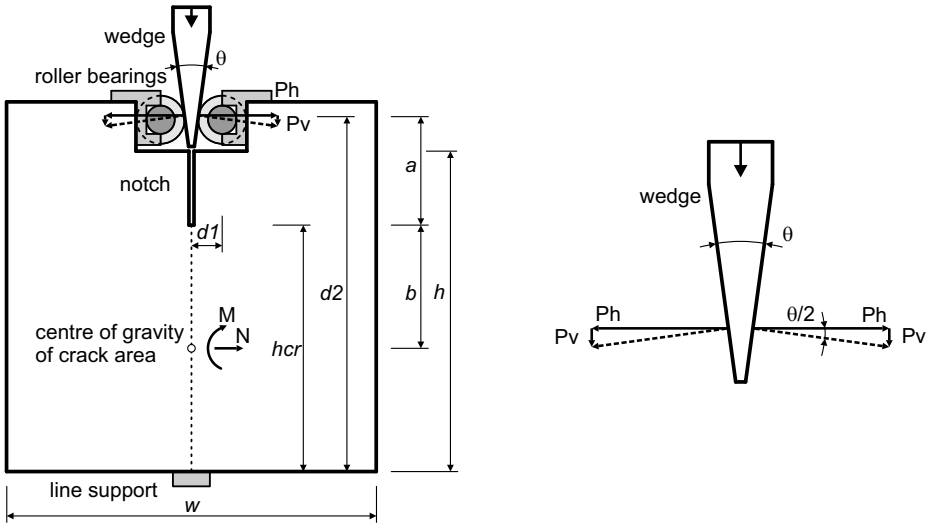


Figure 3: Wedge splitting test setup

Utilizing the aforementioned Lattice Discrete Particle Model, all the experimental investigated tests were numerically simulated. Due to the very close ages of testing, 36 $\sim$ 56 days, and the use of rapid set cement, the test results have very low scatter and thus the aging effect can be neglected. The tests were simulated as one concrete material and the average experimental results were utilized as reference.

Aggregate size range of 8 $\sim$ 16 mm is applied to generate randomly the lattice discrete particles. The maximum aggregate size of 16 mm is obtained from the concrete composition. The minimum aggregate size of 8 mm is selected as half of the maximum aggregate size to save computational cost. The material test results of concrete C50 under compression, splitting and modulus tests are used for calibration and validation of LDPM simulations, as shown in Fig. 4 $\sim$ 6. The calibrated LDPM mesoscale parameters for C50 are listed in Table 2.

Table 2: LDPM Mesoscale Parameters for Concrete C50

| | |
|---|---|
| NormalModulus [MPa] | 84000 |
| TensileStrength [MPa] | 4.8 |
| CompressiveYieldingStress [MPa] | 240 |
| ShearStrengthRatio [-] | 2.7 |
| TensileCharacteristicLength [mm] | 300 |
| SofteningExponent [-] | 0.4 |
| InitialFriction [-] | 0.4 |

The normal modulus is calibrated by matching the experimentally measured $E$ modulus extracted from the compression test stress-strain curves and also the linear branch of WST force-CMOD curves, see Fig. 4 & 6. Note that the WST tests are performed on 28 days of age using a batch of specimens with different temperature and relative humidity evolutions, than the other specimens used for material tests. The simulated WST responses fall into the range of those of the experiments, although relatively stiffer behavior in the linear section is observed in the experimental responses. The strength related parameters, e.g. tensile strength, compressive yield stress, shear strength ratio, are calibrated by matching the experimental peaks of compression and splitting tests. Initial friction is calibrated by compressive response. The fracture related parameters, including the tensile characteristic length and softening exponent, are calibrated based on the post peak strain softening behavior from wedge splitting tests. The other parameters' values are determined based on calibrated sets for typical concrete materials available in the literature [41, 42]. The adopted values are densification ratio = 2.5, alpha = 0.25, asymptotic friction = 0, initial hardening modulus ratio = 0.4, transitional strain ratio = 4, transitional stress = 300 MPa, volumetric deviatoric coupling coefficient = 0, deviatoric strain threshold ratio = 1, and deviatoric damage parameter = 5.

As shown in Fig. 4 - 6, the numerical results match those of the experiments for: compressive strength,

tensile prism splitting strength, wedge splitting strength, the Young's modulus measured from compression and WST, as well as post-peak behavior representing fracture energy. Furthermore, the set of parameters are also used for prediction of structural scale shear beam tests with promising results [49], thus they are considered calibrated and validated.

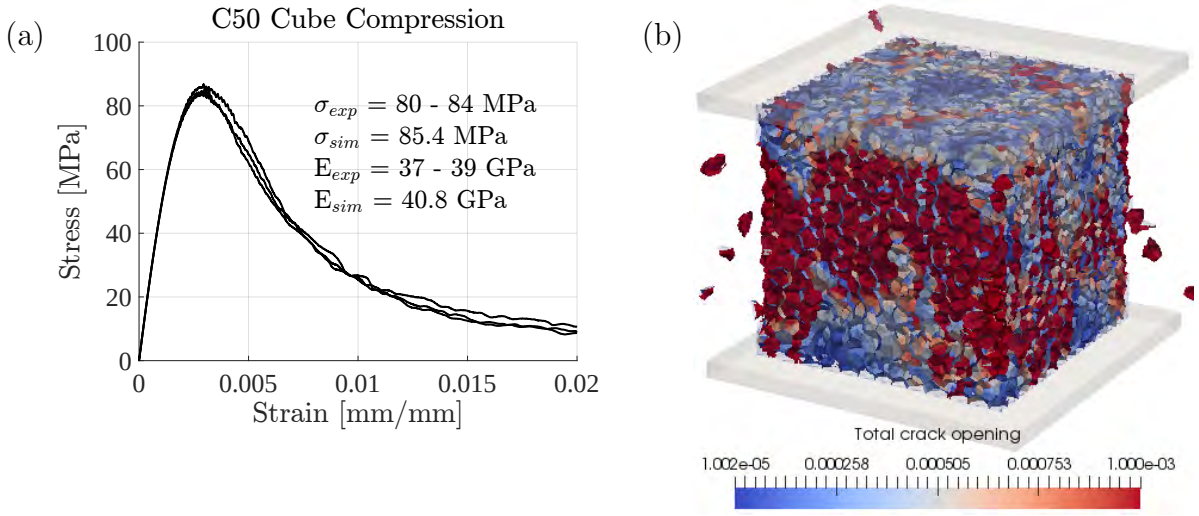


Figure 4: LDPM simulations of unconfined cube compression for C50 (a) experimental and simulated results (b) simulated postpeak crack pattern

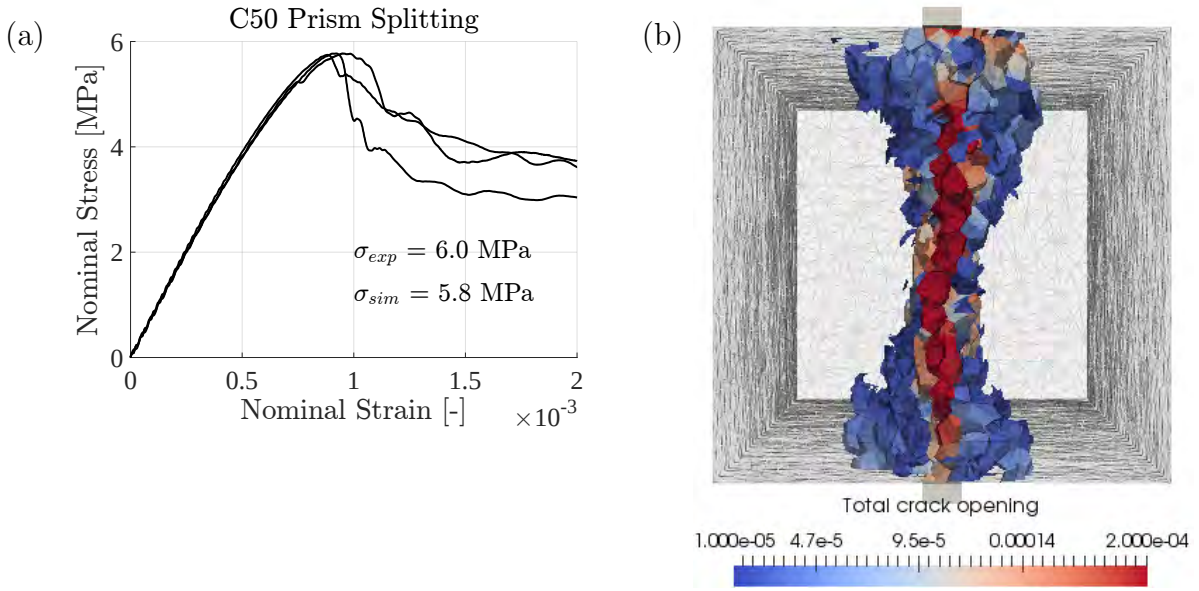


Figure 5: LDPM simulations of prism splitting test for C50 (a) experimental and simulated results (b) simulated postpeak crack pattern

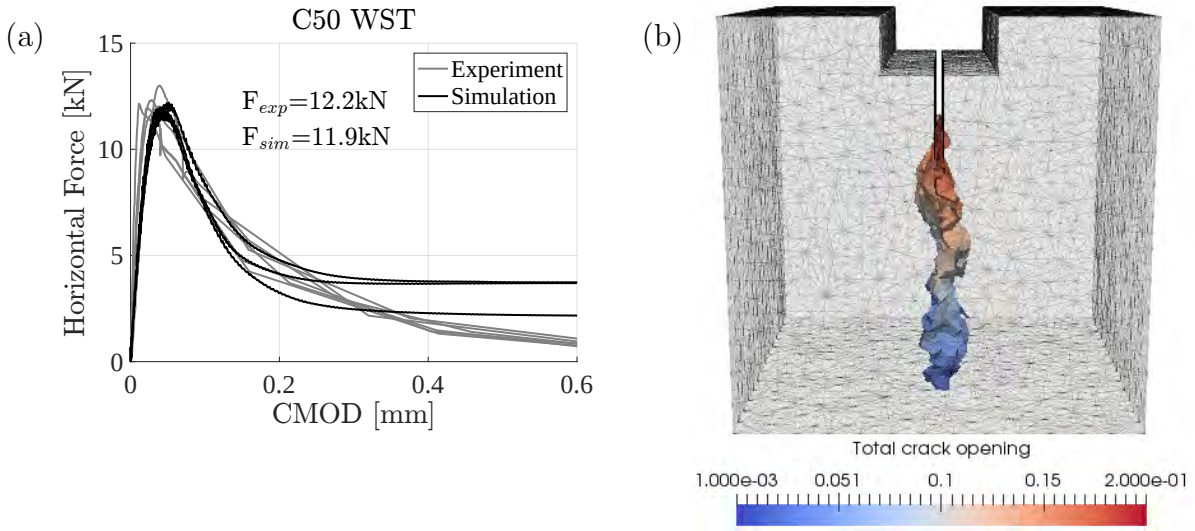


Figure 6: LDPM simulations of wedge splitting test for C50 (a) experimental and simulated results (b) simulated postpeak crack pattern

### 2.2 LDPM Calibration for Ultra high performance concrete

The ultra high performance concrete selected in this study is taken from the literature [55] and has constituents as listed in Table 3. In the study, the LDPM parameters were extensively calibrated and validated for the UHPC based on experimental tests including unconfined uniaxial compression, triaxial compression, 3-point bending, 4-point bending of different sizes, and splitting tensile test. The compression and splitting tests were conducted on cored cylindrical specimens having lengths of 102 mm and diameters of 51 mm. The bending test beams had sizes of 356 mm to 1016 mm in length, 25 mm to 102 mm in height, and constant width of 102 mm. The simulated stress-strain and load-displacement relations well match those of the experiments. As examples, the simulation results of bending and compression tests are displayed in Fig. 7. As shown, the numerical and experimental stress-strain curves overlap with each other for compression test. With the proven ability of predicting mechanical behavior of the UHPC [55], the LDPM can be reliably used to analyze the size effect in compression of specimens with different geometries. The particle size range from 2 to 4 mm was used in the model, instead of the actual particle size up to 0.6 mm, to save computational cost. This approach belongs to the Coarse Graining (CG) methods that are formulated to reduce the computational cost of discrete fine-scale models. The CG method is based on constructing a model with a reduced number of degrees of freedom that preserves the same mathematical and computational structure of the original model. From the computational point of view the CG decreases

the number of degrees of freedom with fewer calculations per time step, and increases the spatial resolution of the system which allows larger stable time step in explicit solvers as in LDPM. CG is widely used in the field of atomistic simulations and molecular dynamics [66]. Moreover, CG was also successfully adopted in many LDPM numerical studies [55], and its efficiency and accuracy has been verified by simulating several examples, see [67, 68]. The adopted values for the LDPM mesoscale parameters are compressive yielding strength = 500 MPa, initial hardening modulus ratio = 0.36, densification ratio = 2.5, transitional strain ratio = 2, shear strength ratio = 17, initial friction = 0.5, softening exponent = 0.2, transitional stress = 300 MPa, tensile strength = 4, and tensile characteristic length = 150 mm [55].

Table 3: Constituents and Mixing Proportions of UHPC CorTuf

| Ingredient | Type | Proportion | Weight per kg |
|---|---|---|---|
| Cement | Lafarge Type H | 1.0000 | 0.3497 |
| Sand | F-50 | 0.9674 | 0.3383 |
| Silica Flour | Sil-co-sil 75 | 0.2768 | 0.0968 |
| Silica Fumes | Elkem ES-900W | 0.3890 | 0.1360 |
| Superplasticizer | ADVA-190 | 0.0180 | 0.0063 |
| Water | Tap Water | 0.2082 | 0.0728 |

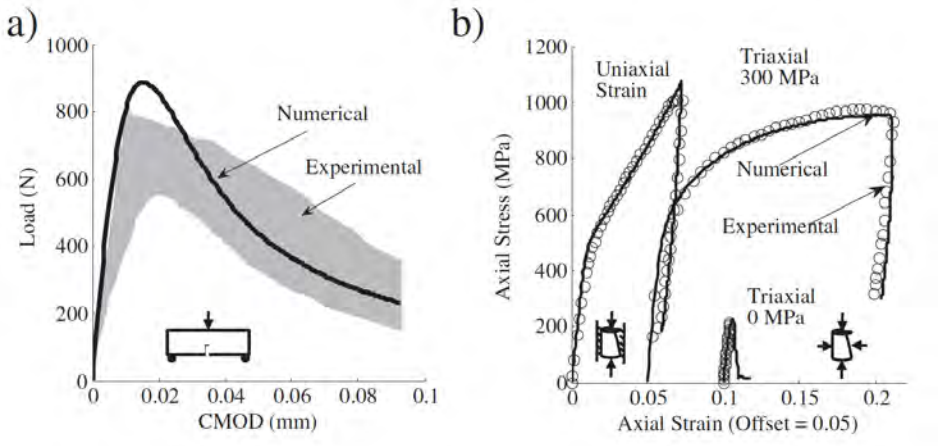


Figure 7: LDPM simulations of UHPC CorTuf (a) 3-point bending (b) uniaxial strain and triaxial compression [55]

## 3 Numerical analysis of size effect in compression

LDPM is able to simulate accurately the behavior of concrete under unconfined compression, as demonstrated in [41], reproducing with great accuracy the effect of specimen length (stronger and more ductile behavior for shorter specimens) and the effect of frictional boundary conditions on compressive strength, post-peak ductility, and failure mode (splitting cracks for low friction condition and shear-band type fracture for high friction conditions). LDPM succeeds in this difficult task without postulating compressive softening behavior in the mesoscale constitutive equations, i.e. the macroscale softening behavior for unconfined compression is governed mainly by tensile fracturing and cohesive/frictional shearing at the meso-scale, consistently with well known experimental evidences, see e.g. [6].

After obtaining the mesoscale LPDM parameters by extensive calibration and validation, the LDPM is here utilized to simulate the compressive behavior of the two adopted concretes for different specimen sizes. Both of the two common geometries as in the laboratory tests, prisms and cylinders, are used in the numerical analysis. The typical experiments conducted under uniaxial unconfined compression load are simulated and presented in this section. The load is applied through steel platens that are either directly in contact with the specimens ends (high friction condition) or the contact surface are treated to reduce friction (low friction condition), such as with teflon sheets. Since the two conditions, low and high friction, influence differently the compressive behavior, both of them are considered in the numerical analysis. To simulate friction between the specimen ends and the steel loading platens, a slippage-dependent friction coefficient has been formulated as $\mu(s) = \mu_d + (\mu_s - \mu_d)s_0/(s_0 + s)$ [38, 41]. For high friction condition the following values are utilized: $\mu_s = 0.13$, $\mu_d = 0.015$, and $s_0 = 1.3$ mm, as calibrated for untreated loading platens in [41]. While for low friction condition, the utilized values are $\mu_s = 0.03$, $\mu_d = 0.0084$, and $s_0 = 0.0195$ mm, which represent the contact surface covered with teflon sheets to reduce friction between concrete and steel platens, as calibrated in [41] using data from [69]. The loading setup and typical surface mesh are shown in Fig. 8.

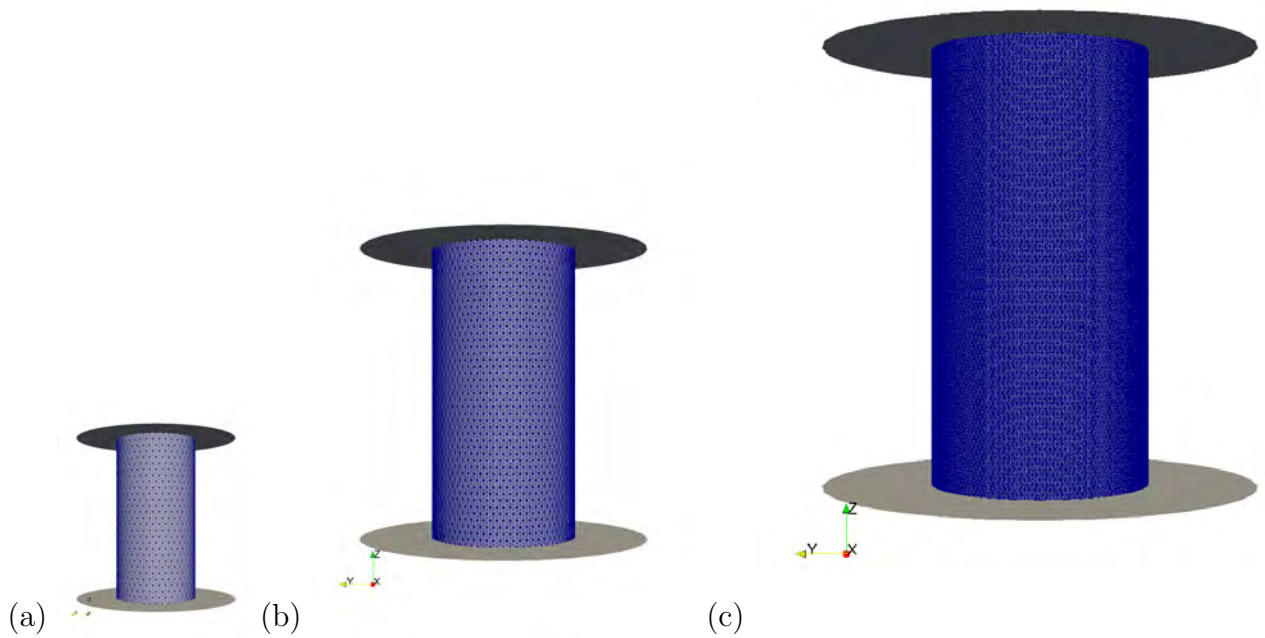


Figure 8: LDPM compression test setup of UHPC specimens (a) 50x100 (b) 100x200 (c) 200x400 mm

The compression failure at the microscale is characterized by several different mechanisms such as (1) microcracks originating from pores; (2) microcracks generated by inclusions stiffer than the mortar matrix; (3) wing-tip microcracks originated by the slip on an inclined crack that gradually turning into the direction of compression; (4) local crushing in the weaker interfacial transition zone; (5) aggregate/matrix de-bonding cracks initiated by differential temperatures from hydration, differential shrinkage and excessive bleeding near aggregates. All these microscopic mechanisms can explain the appearance of microcracks and local damage under compression loading but they cannot explain the global fracture and compressive failure. Macroscopic splitting cracks, which often occur in small laboratory test specimens when the end cross sections are sliding with negligible friction, do not cause global energy release. Because of the absence of a global energy release, this type of compression failure cannot cause any size effect, as confirmed by several numerical results [2, 56, 57]. On the macroscale only global fracture mechanisms that cause energy release lead to size effect.

The LDPM approach is capable of simulating all the initial microcracking under mechanical loading since when all the particles are loaded uniformly, and depending on the particle interactions, compressive, tensile or shear stress concentrations will appear in the LDPM geometry. With the microcracking mecha-

nisms, macrocracks originate in the material, for which LDPM simulates very well from the initiation up to the complete failure. With the well calibrated mesoscale parameters of the studied concretes and the friction coefficients allowing contact slippage with loading platens, LDPM simulates very well the compression failure of concretes with different specimen sizes and boundary conditions. In the subsequent sections the simulated results for normal strength concrete and UHPC are presented. For each test, at least three different seeds and consequently three different sets of random particle placement (meso-structure) are used to obtain the LDPM response. Detailed comments on the failure modes are reported in Section 3.3.

### 3.1 Normal Strength Concrete

The simulated compressive strengths of normal concrete C50 are listed in Table 4 and Table 5 for prisms and cylinders respectively. Aspect ratio, $s$, ($s = H/D$, where $H$ is the specimen height and $D$ is the diameter or the side of the cross section) ranging from 1 up to 16 and width dimensions, $D$, of 150, 300, 600 mm have been investigated using high friction condition. The same particle size is kept for the various specimen dimensions, with the consequence that the largest specimens have more than one million elements and the large aspect ratios couldn't be fully simulated. With low friction condition only aspect ratio 1 was as well simulated. The specimens that belong to each group with the same aspect ratio are geometrically similar. The stress-strain curves for prisms and cylinders are shown in Fig. 9 and Fig. 10 respectively. For the sake of direct comparison, the stress-strain curves are organized in groups of aspect ratio and dimension of diameter/width. In order to have an overview of the strengths for all the investigated geometries, the results are also presented in 3-D plots of strengths. vs. diameter/width vs. aspect ratio as shown in Fig. 11. The size effect and shape effect are analyzed in the following sections. In general, higher aspect ratio and larger specimen size lead to more brittle failure. For example, as shown in Fig. 9d, ductile post-peak behavior is well captured for aspect ratio from 1 to 4, whereas the specimen displays pure-brittle failure mechanism for higher aspect ratio.

Table 4: C50 Prism Compressive Strength [MPa]

| Friction | Aspect Ratio | Width 150 mm | Width 300 mm | Width 600 mm |
|---|---|---|---|---|
| High | 1 | 85.4 | 80.0 | 74.2 |
| High | 2 | 65.9 | 61.9 | 61.0 |
| High | 4 | 53.9 | 52.8 | 52.3 |
| High | 8 | 53.9 | n/a | n/a |
| High | 16 | 53.7 | n/a | n/a |
| Low | 1 | 57.9 | 57.3 | 56.5 |

Table 5: C50 Cylinder Compressive Strength [MPa]

| Friction | Aspect Ratio | Diameter 150 mm | Diameter 300 mm | Diameter 600 mm |
|---|---|---|---|---|
| High | 1 | 75.4 | 73.6 | 70.4 |
| High | 2 | 61.1 | 60.1 | 58.9 |
| High | 4 | 54.3 | 52.9 | 52.6 |
| High | 8 | 53.7 | n/a | n/a |
| Low | 1 | 54.6 | 54.9 | 54.3 |

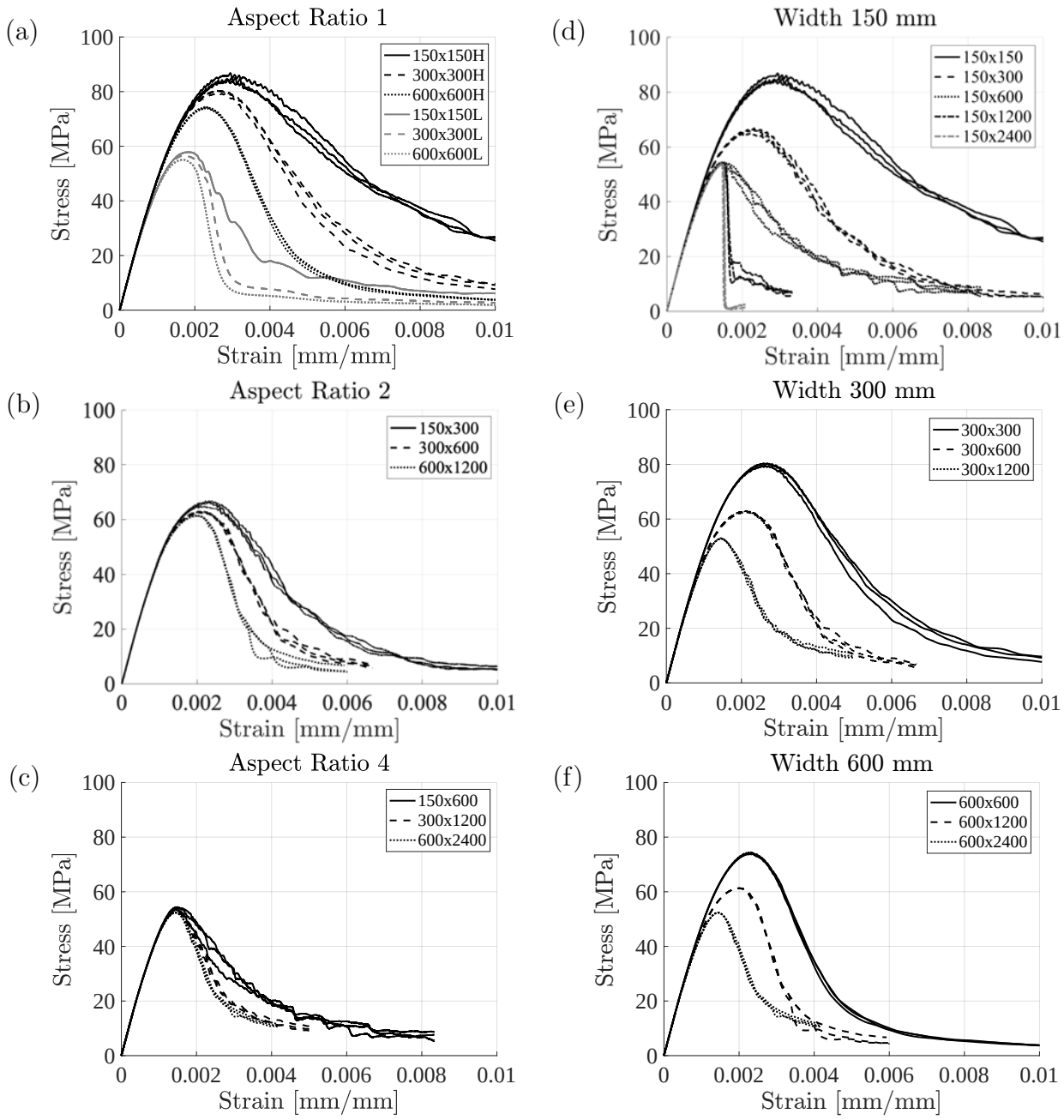


Figure 9: Macroscopic stress-strain curves for unconfined compression of C50 prisms.

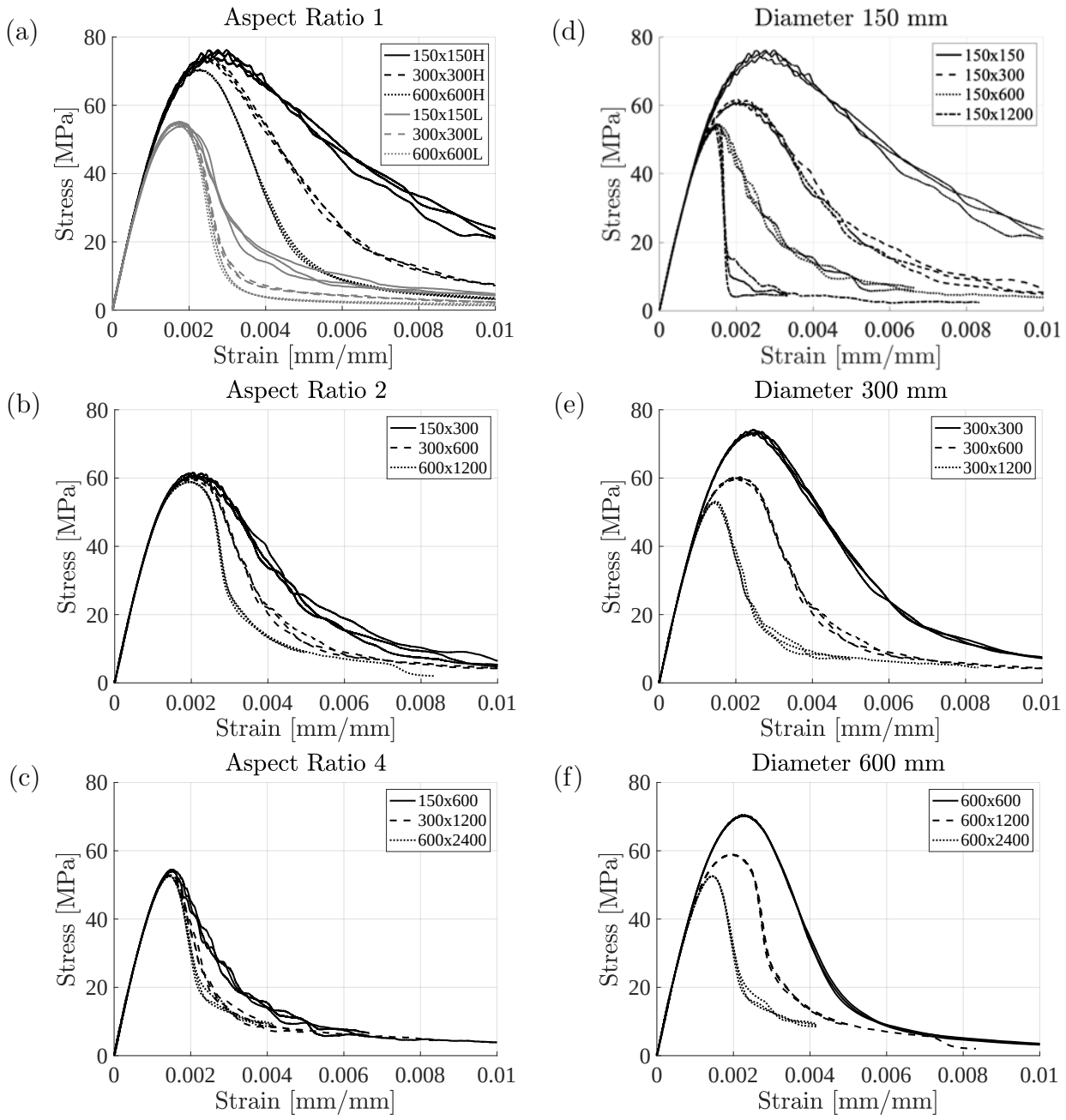


Figure 10: Macroscopic stress-strain curves for unconfined compression of C50 cylinders.

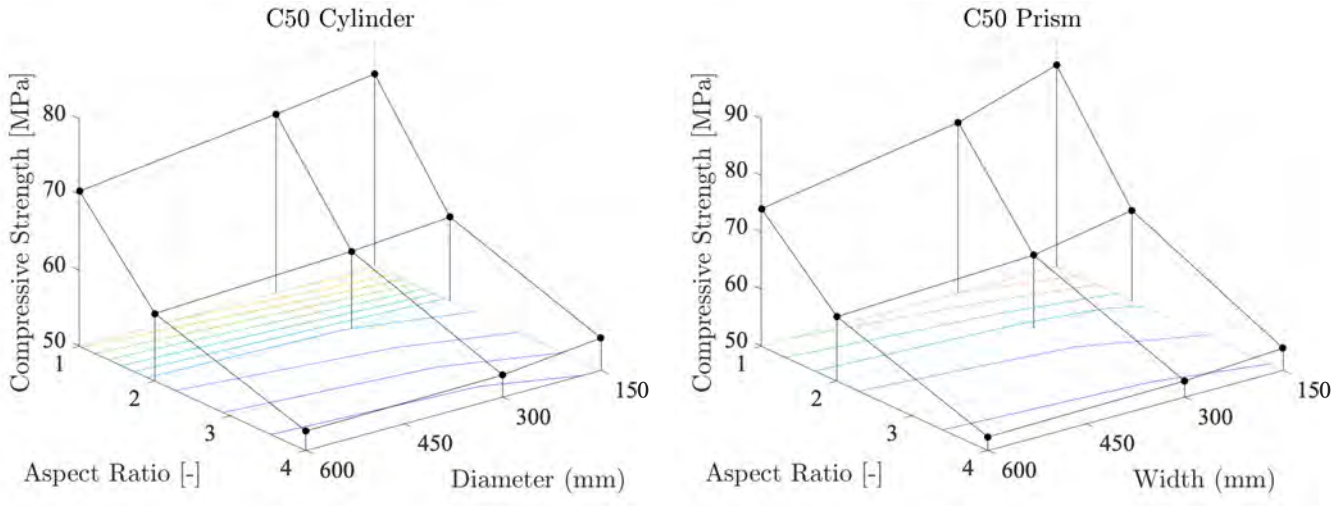


Figure 11: Size Effect 3-D plot of C50 cylinders and prisms

### 3.2 UHPC

The simulated compressive strengths of the UHPC are listed in Table 6 and Table 7 for cylinders and prisms respectively. Aspect ratio ranging from 1 up to 4 and diameter/width dimensions of 50, 100, 200 mm have been investigated with high friction. While with low friction condition specimens with aspect ratio 1-4 have been as well simulated. The stress-strain curves for UHPC prisms and cylinders are shown in Fig. 13-14. In order to directly compare the strengths, the stress-strain curves are organized in groups of aspect ratio and diameter/width. An overview of the strengths for all the investigated geometries is useful and the results are presented in 3-D plots of strengths. vs. diameter/width vs. aspect ratio as shown in Fig. 15. The UHPC displays a similar trend as the C50 whereas overall has a more brittle failure than C50. While ductile post-peak behavior is shown for aspect ratio 1 and 2, the post-peak curve shows almost no softening for aspect ratio 4. More detailed size effect and shape effect are analyzed in the following sections.

Table 6: UHPC Cylinder Compressive Strength [MPa]

| Friction | Aspect Ratio | Diameter 50 mm | Diameter 100 mm | Diameter 200 mm |
|---|---|---|---|---|
| High | 1 | 302.4 | 292.1 | 287.4 |
| High | 2 | 245.9 | 242.9 | 239.6 |
| High | 4 | 229.6 | 229.0 | 227.1 |
| Low | 1 | 245.0 | 237.3 | 236.4 |
| Low | 2 | 236.3 | 234.3 | 232.1 |
| Low | 4 | 230.6 | 230.8 | 228.8 |

Table 7: UHPC Prism Compressive Strength [MPa]

| Friction | Aspect Ratio | Width 50 mm | Width 100 mm | Width 200 mm |
|---|---|---|---|---|
| High | 1 | 308.0 | 300.0 | 293.4 |
| High | 2 | 251.0 | 245.5 | 245.1 |
| High | 4 | 223.7 | 223.9 | 224.4 |

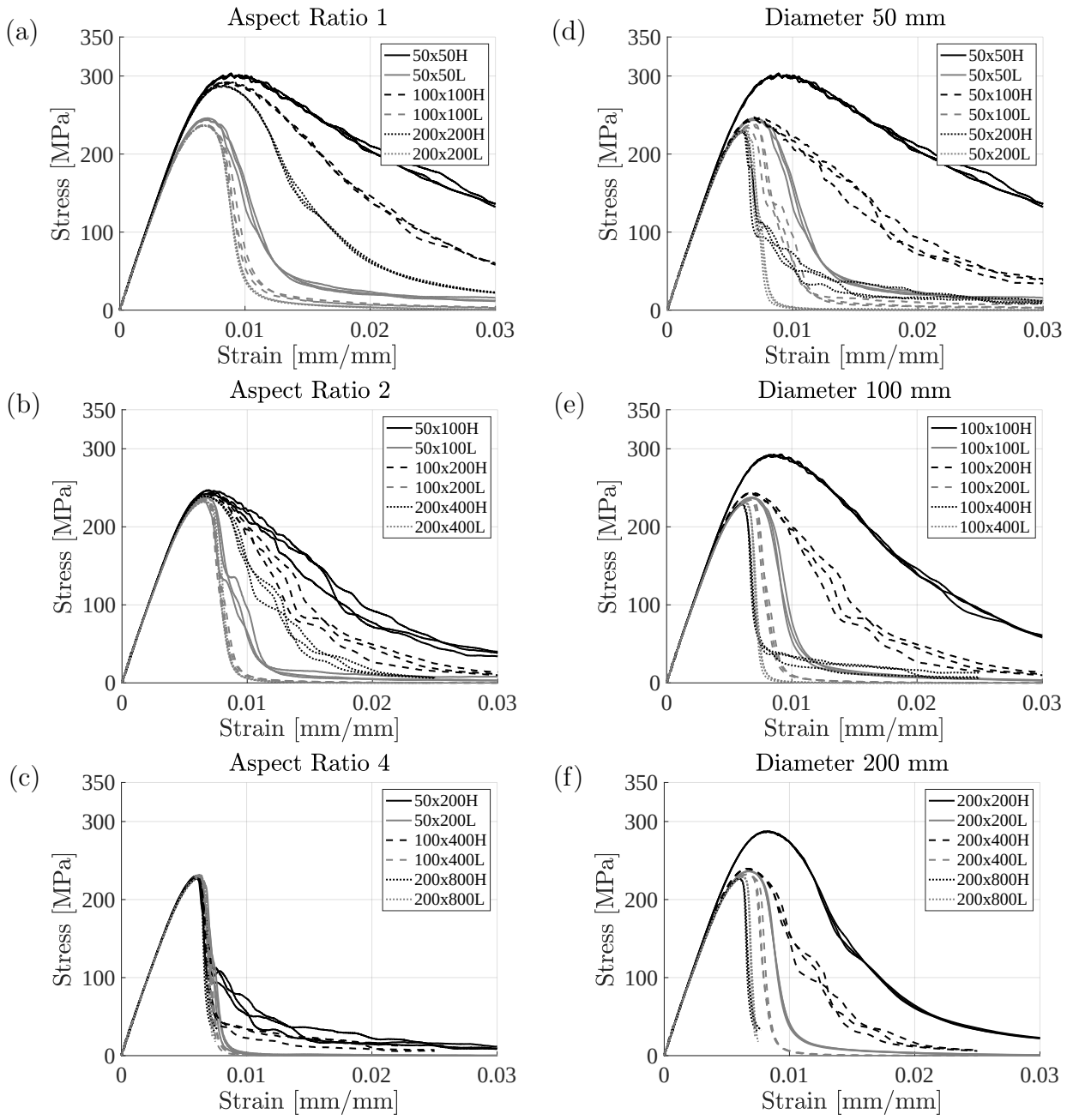


Figure 12: Macroscopic stress-strain curves for unconfined compression of UHPC cylinders.

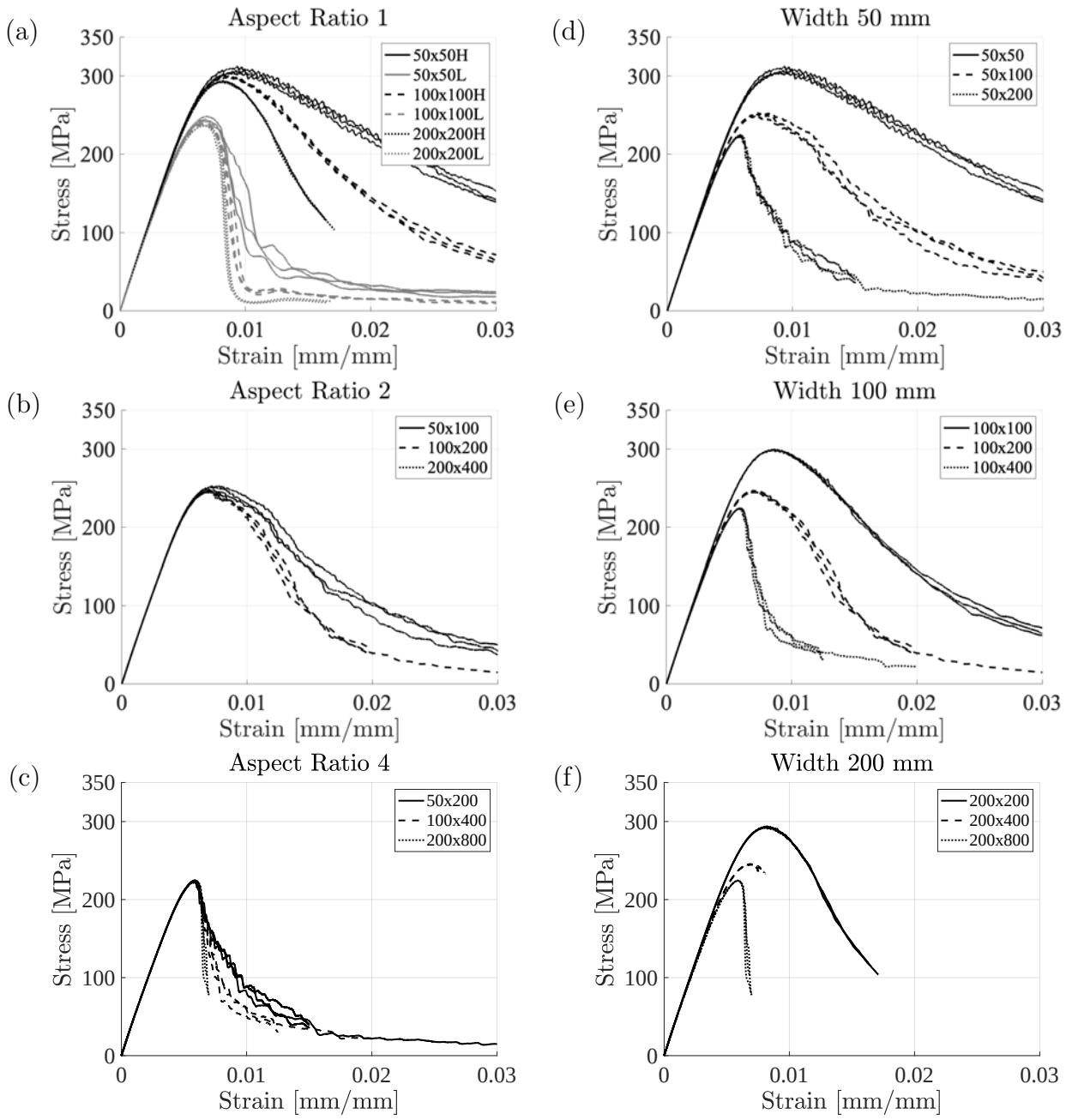


Figure 13: Macroscopic stress-strain curves for unconfined compression of UHPC prisms.

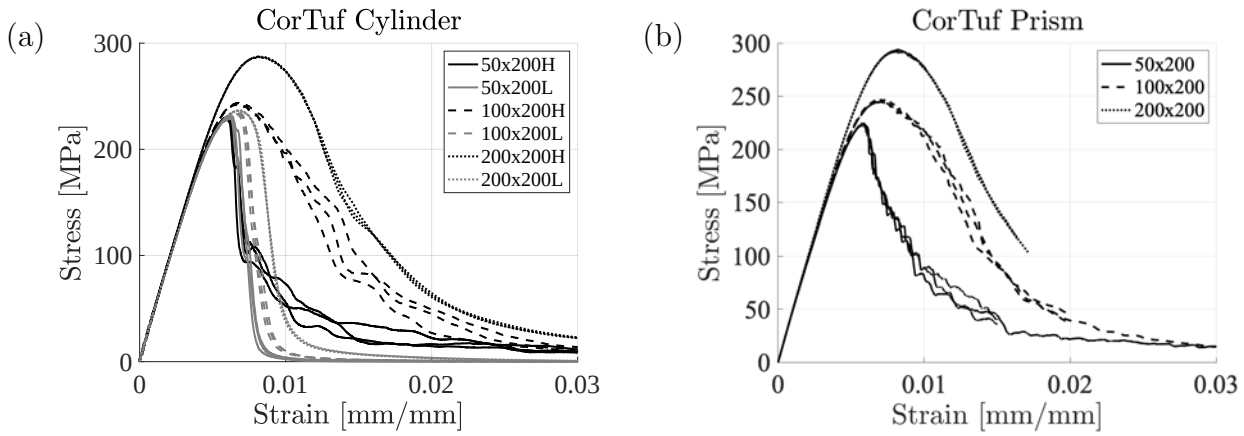


Figure 14: Comparison of macroscopic stress-strain curves for unconfined compression of UHPC cylinders (a) and prisms (b) with the same height.

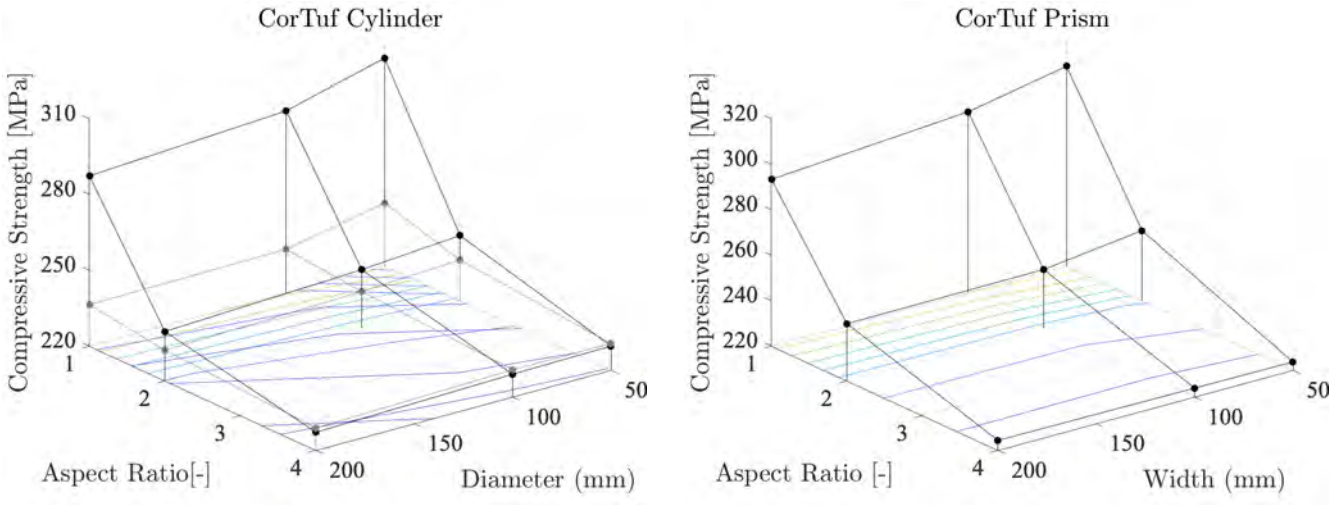


Figure 15: Size Effect 3-D plot of UHPC cylinders and prisms.

### 3.3 Observed Failure Modes

The failure mechanisms of the simulated specimens by LDPM are discussed in this section. In general, vertical splitting cracks form under low friction conditions, while both splitting and transverse cracks occur forming cone shapes on the two ends for high friction situations. Under low friction, the end cross sections are sliding with negligible confinement. The resultant macroscopic splitting cracks do not cause global energy release and consequently no size effect. On the other hand, transverse propagation of a cracking band (or damage band) observed under high friction contributes to a global energy release and thus displays size effect. In actual experiments, such transverse cracking may be triggered or accompanied by an internal buckling caused by microcracks that weaken the material [17, 62, 63].

Fig. 16-23 show the detailed failure types simulated by LDPM for C50 and UHPC under low and high friction conditions for the studied geometries. There is no distinguishable difference in the crack pattern between prism and cylinder, since for both shapes well-defined cylindrical cones form on the two ends under high friction. One exception is for UHPC aspect ratio equal to 1, shown in Fig. 19, when the cube seems to have a more elliptical shape of the cone when compared to the cylinder. To give a closer look at the crack propagation, the crack patterns at different stages before peak and post-peak of cylinder and prism specimens are shown in Fig. 24-26. The initial micro-cracks seem to emerge at the edges of the specimen which then grow inward and leaving parabolic or elliptical cones intact on the two ends.

The failure mechanisms of NSC and UHPC generally agree with each other. The two concretes have very different aggregate sizes, which are up to 16 mm for C50 and only 4 mm for UHPC, as modelled by LDPM. Despite that the studied specimen size of C50 is 3 times larger than that of UHPC, the modelled UHPC specimens have relatively more particles, larger number of degrees of freedoms, and hence may give more detailed and localized crack patterns. A comparison of the particle size and the specimen size between NSC and UHPC is presented in Fig. 8. As seen, the particle size has 4 times difference while the specimen size has 3 times difference between NSC and UHPC. Thus the relative difference between NSC and UHPC is limited, e.g. the ratio of specimen size to particle size are on about the same magnitude. The numerical specimen sizes are based on the utilized experimental specimen sizes. In addition there are experimental and numerical limits: if the NSC size is too small, the number of aggregates or particles will be also too limited; if the UHPC specimen size is too large, it will be challenging also for the experimental capacity and the computational cost. As a result, the difference in the failure pattern figures due to just particle size is limited. The focus of comparison is rather the failure patterns due to high and low friction conditions, plus the difference of cracking area of specimens with different aspect ratio.

Table 8: Particle size and specimen size comparison of NSC and UHPC

| | particle size [mm] | | specimen size [mm] | | ratio |
|---|---|---|---|---|---|
| | min | max | min | max | |
| NSC | 8 | 16 | 150 | 600 | 37.5 |
| UHPC | 2 | 4 | 50 | 200 | 50 |

Looking at the crack patterns of all studied specimens, the cones seem to have a slant angle, measured from slant to radius, ranging from about 40 to 60 degrees, while the majority of all specimens have a slant

angle of 60 degrees. Note this is more than the typically assumed 45 degree angle for such cone failure in compression. The slant angle tend to increase with rising aspect ratio. When aspect ratio s=4, the cone starts from the very edges on one end to just before reaching the mid-height. While for low aspect of s=1 and s=2, the two ends of the specimen get crushed from edges toward the center, the specimens with s=4 have the two ends nearly intact. Seeing that size effect diminishes for high aspect ratio, e.g. when s=4, this supports the theory that deterministic size effect in compression in mainly caused by the confinement on the two ends due to high friction with loading platens. For this reason, the confinement is seemingly not felt by the high aspect-ratio specimen and thus the failure mechanism is without size effect. Whereas with low aspect ratio, the failure is governed by the confinement, and consequently exhibits relatively high size effect.

In real reinforced concrete structures, compressive failure occurs typically under the effect of some confinement as a consequence of the effect of the steel reinforcement (at least the minimum amount) and some shear/bending actions. This is the reason why the size effect under high friction condition is much closer to real loading conditions and, consequently, is of primary importance in RC structures [2, 64].

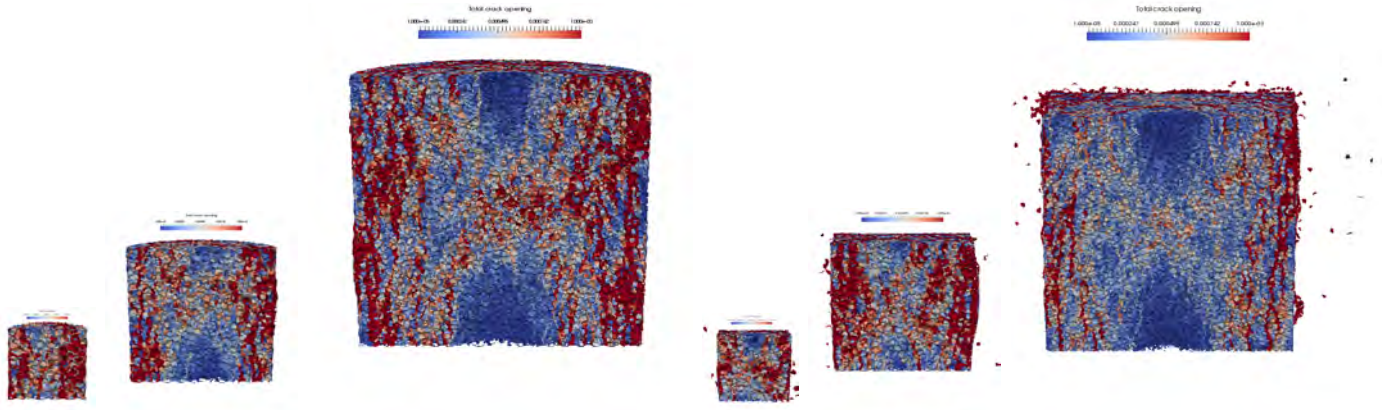

Figure 16: C50 Cylinder and Cube Aspect Ratio 1 High Friction Simulated Failure Types

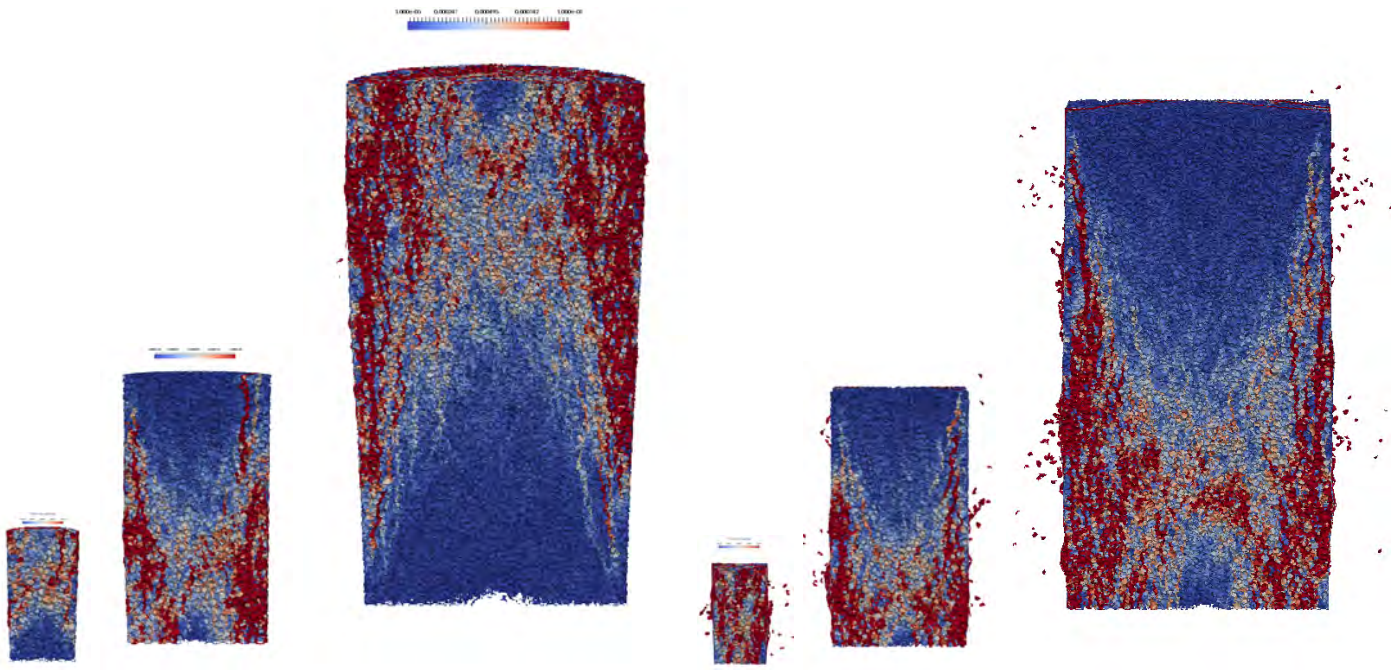

Figure 17: C50 Cylinder and Prism Aspect Ratio 2 High Friction Simulated Failure Types

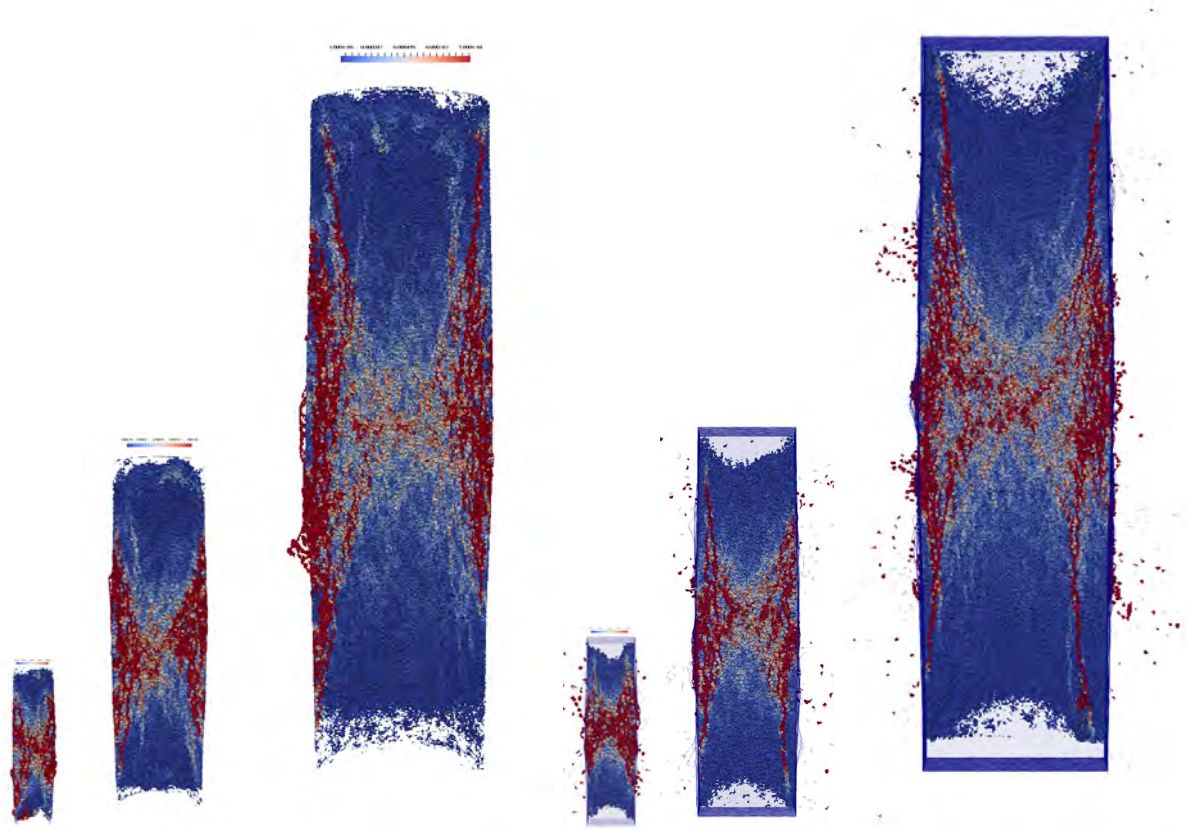

Figure 18: C50 Cylinder and Prism Aspect Ratio 4 High Friction Simulated Failure Types

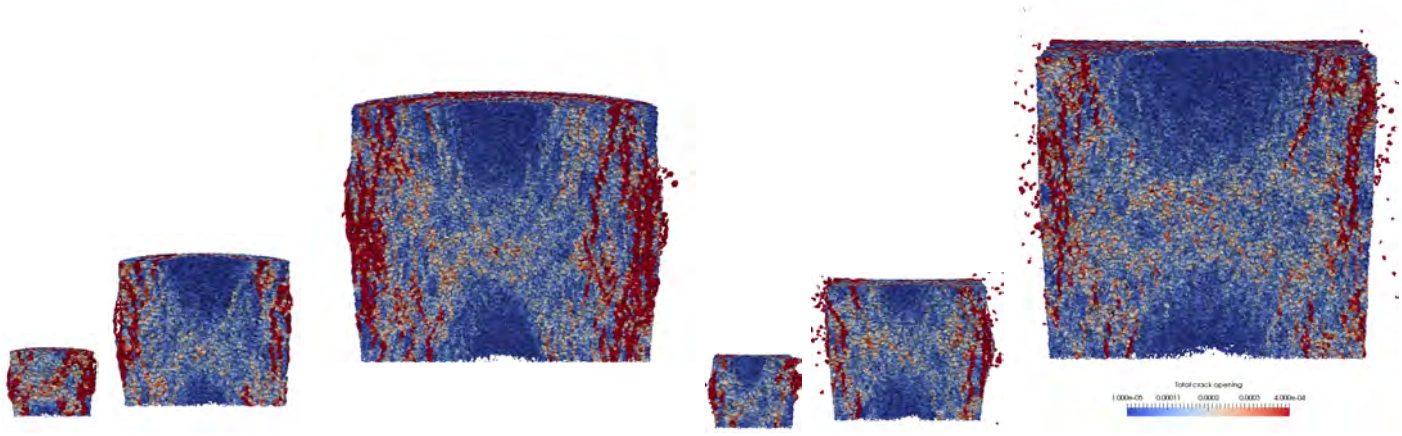

Figure 19: UHPC Cylinder and Cube Aspect Ratio 1 High Friction Simulated Failure Types

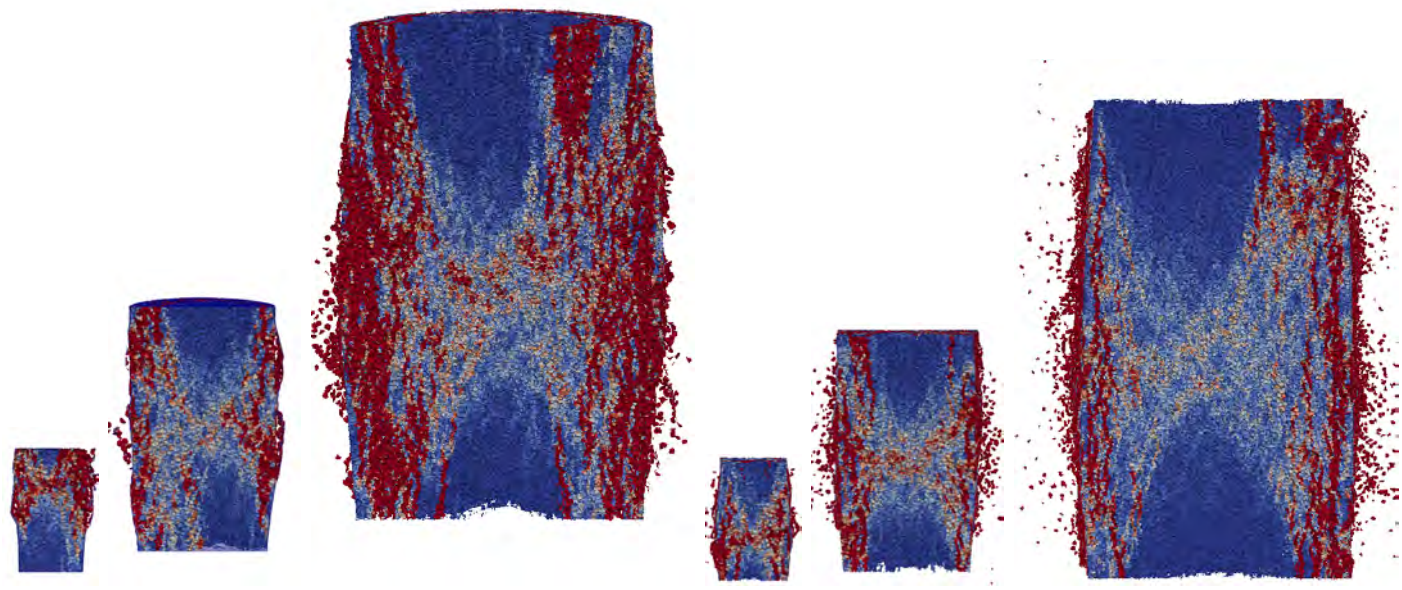

Figure 20: UHPC Cylinder and Prism Aspect Ratio 2 High Friction Simulated Failure Types

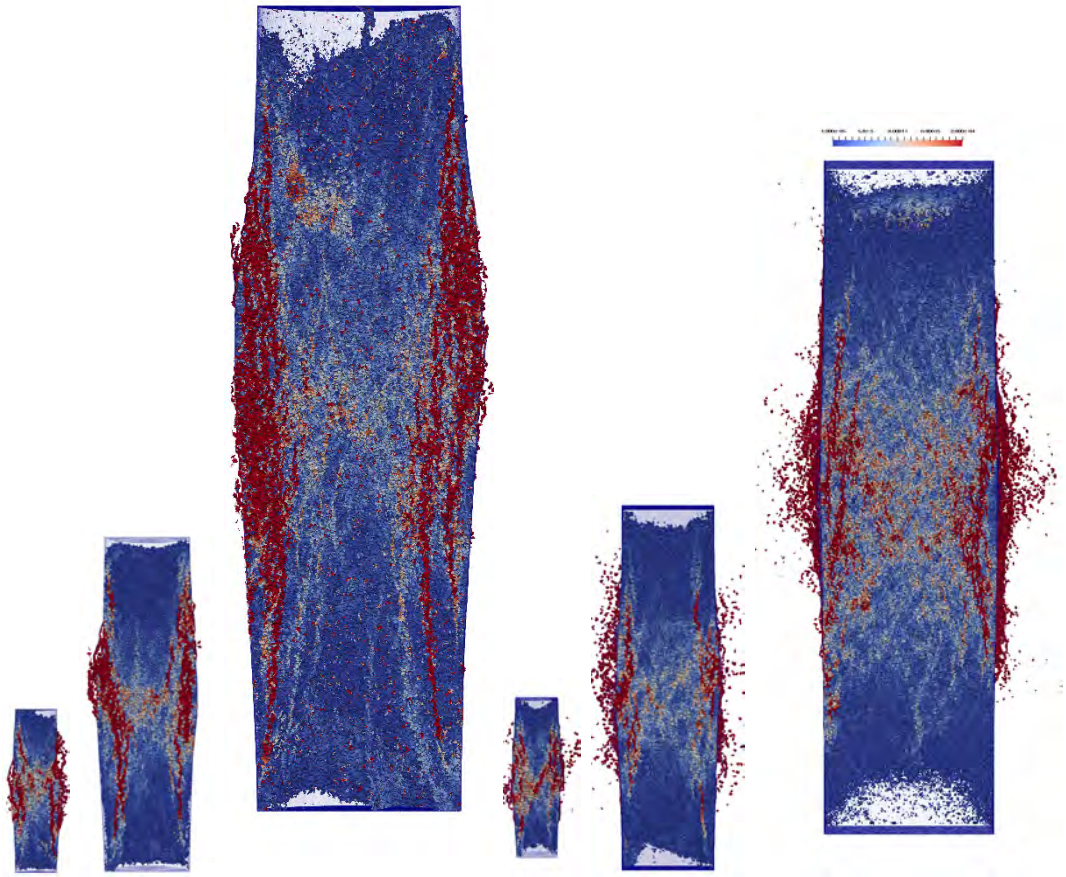

Figure 21: UHPC Cylinder and Prism Aspect Ratio 4 High Friction Simulated Failure Types

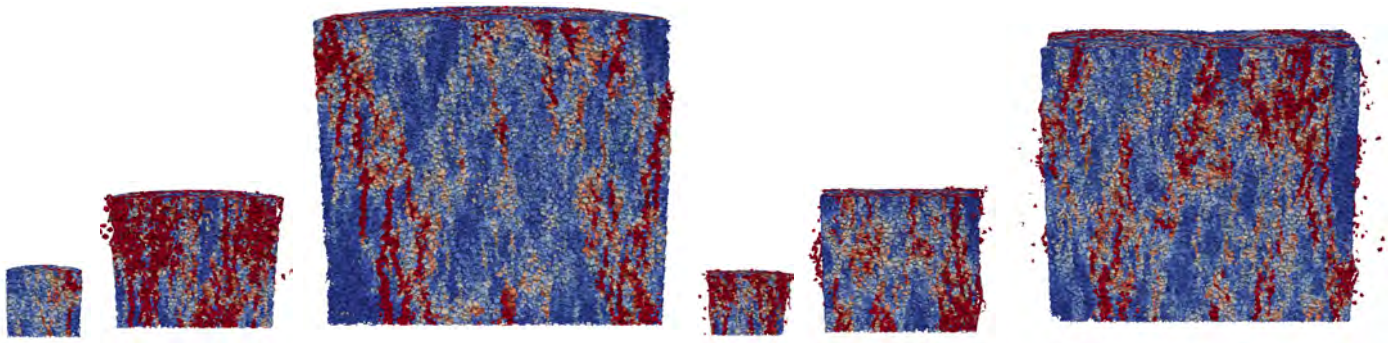

Figure 22: UHPC Cylinder and Cube Aspect Ratio 1 Low Friction Simulated Failure Types

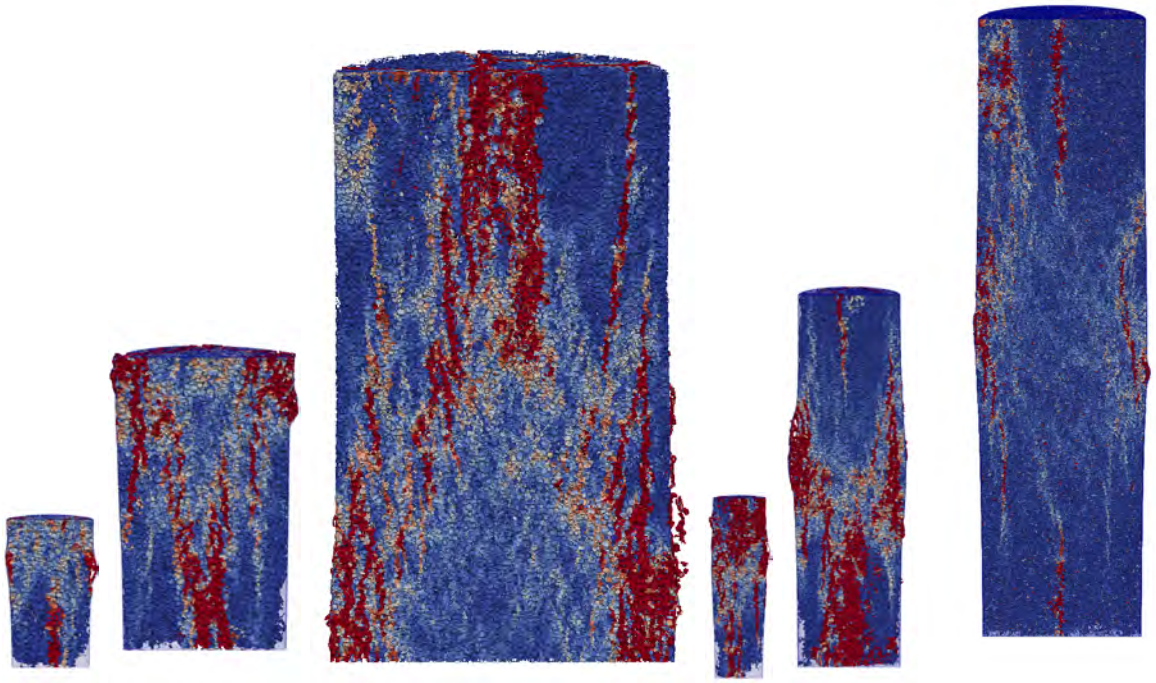

Figure 23: UHPC Cylinder Aspect Ratio 2 and 4 Low Friction Simulated Failure Types

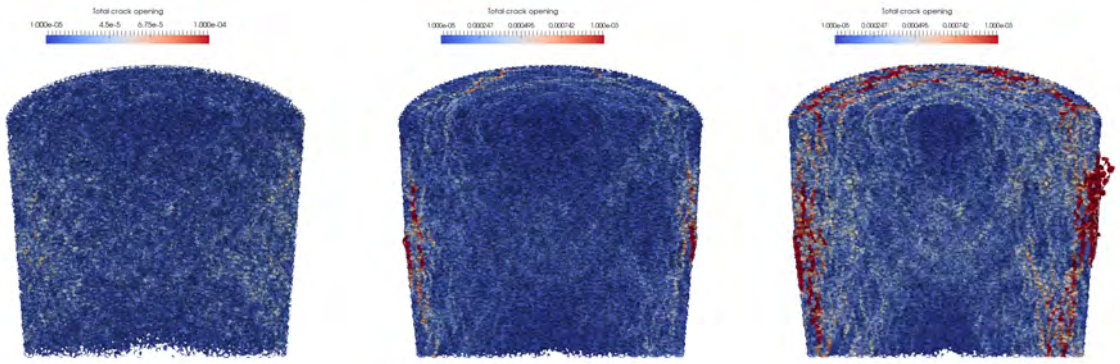

Figure 24: UHPC Cylinder 200x200 mm Crack Propagation at 80% before peak, at peak and 90% post-peak

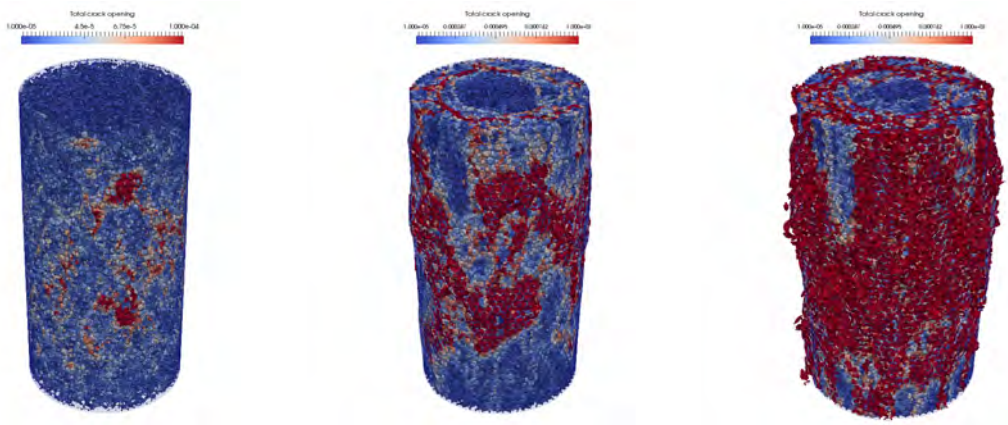

Figure 25: UHPC Cylinder 100x200 mm Crack Propagation at peak, at 90% post peak and 80% post-peak

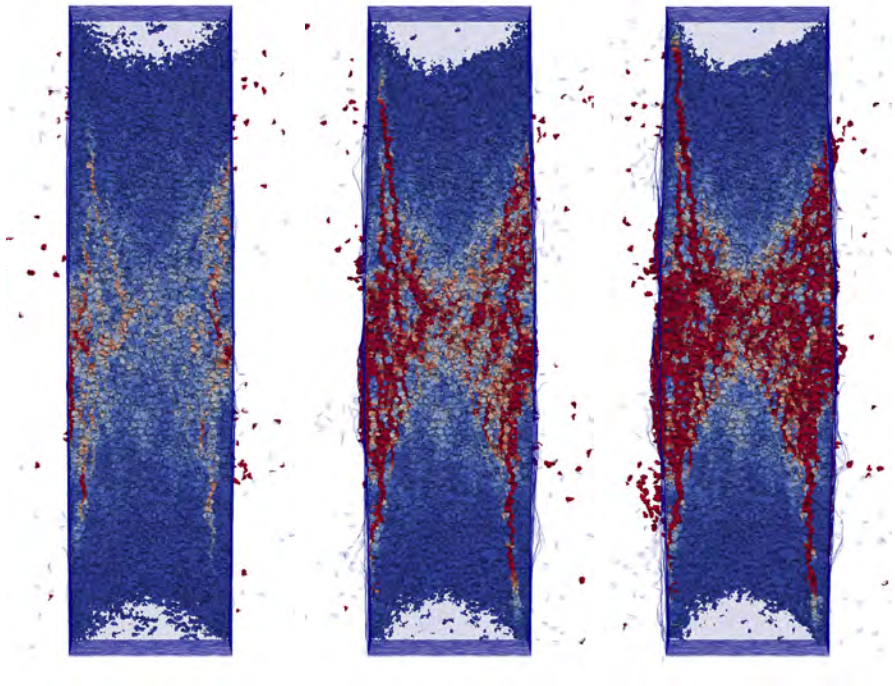

Figure 26: C50 Prism 300x1200 mm Crack Propagation at 50%, 30% and 20% post peak

Fig. 27 shows the stress profiles of the UHPC cylinder of dimensions 200×800 under high friction and low friction conditions. The stress in the horizontal direction XX and vertical direction ZZ are extrapolated shortly after peak at the middle slice of the specimen. These stress profiles correspond to the failure types shown in Fig. 21 under high friction and Fig. 23 under low friction. The main difference lies in the top and bottom sections just next to the supports. The stress XX is more uniform under low friction whereas it exhibits higher values in compression at the two ends due to confinement under high friction loading.

The stress ZZ is closely related to the crack patterns for both high and low friction conditions. When a crack forms, the local resistance against compression decreases. This leaves the cracked sections with lower compressive stresses while the uncracked sections resisting higher stresses. Looking at the top and bottom parts, one can see a cone shape of stress distribution under high friction versus vertical splitting under low friction, which correspond to the crack patterns. The lower stress at the top and bottom under high friction is, however, not due to cracking but a cone shape that is intact due to confinement.

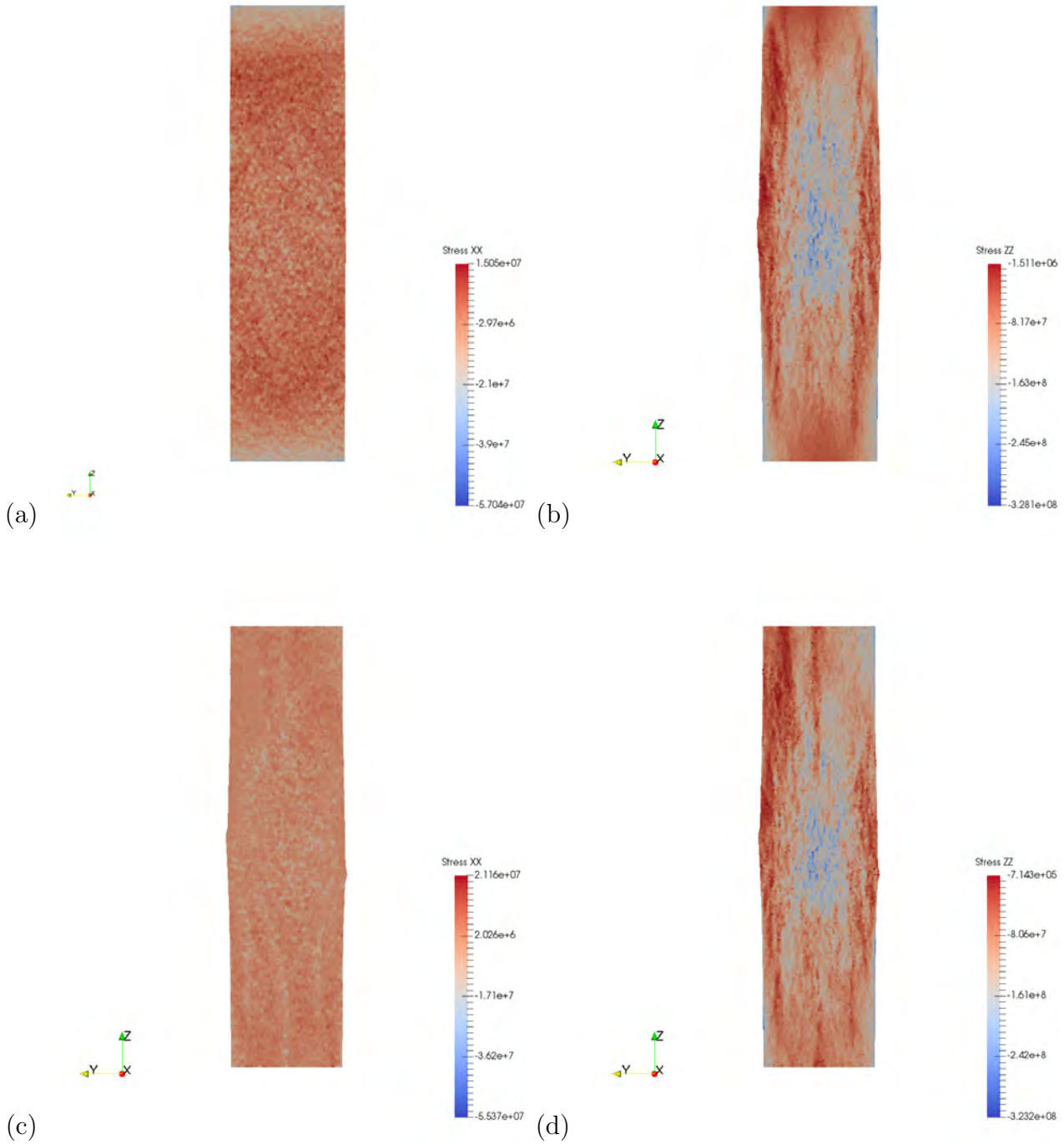


Figure 27: UHPC Cylinder 200×800 stress profiles (a) high friction stress-XX (b) high friction stress-ZZ (c) low friction stress-XX (d) low friction stress-ZZ

## 4 Size Effect Analysis

The well known Size Effect Law (SEL) of Bažant [2] is expressed as

$$\sigma_N = \sigma_0 \left(1 + \frac{D}{D_0}\right)^{-1/2} \tag{2}$$

where $D$ is the characteristic dimension of the structure, $\sigma_0$ and $D_0$ are two constants that have to be evaluated by fitting the data for different sizes. Here $\sigma_N = P_{max}/A$, with $A$ =area of the loaded cross section, is the nominal strength of structure with the dimension of stress, and $P_{max}$ is the maximum load that causes the failure.

The Bažant's SEL catches very well the scale effects under tensile failure. The SEL equation (Eq. 2) is often used for compressive failure, arguing that under compression the failure is the results of local tensile/fracturing mechanisms [2, 64]. However, Bažant and Xiang [63] interpret the compressive failure as the result of the creation and propagation of a band of axial splitting cracks proposed the following relation between the compressive strength and the structural size

$$\sigma_N = C_1 D^{-2/5} + C_0 \tag{3}$$

where $C_1$ and $C_0$ are constants to be determined on the basis of experimental data, and the formula is termed CSEL. This size effect approaches an asymptote of slope -2/5, which means a milder size effect than the classical SEL. The constant $C_0$ represents a residual stress given by the critical stress for internal buckling in the band. Muciaccia et. al. [17] proposed to rewrite Eq. 3 as

$$\sigma_N = \left(\frac{D_0}{D}\right)^{2/5} + f_c^{\infty} \tag{4}$$

where $D_0$ and $f_c^{\infty}$ are positive constants for geometrically similar specimens with $f_c^{\infty}$ representing the nominal strength for a very large (infinite) structure and $D_0$ as a length scale parameter. The size effect law for compression in Eq. 4 is here termed ComSEL.

There are also a limited number of available size effect laws in the literature capable of describing size effect in compression incorporating both the cylindrical/prism shapes and height/aspect ratio. Neville [58]

proposed an empirical size effect formula for low to high strength concrete using cylindrical and prism specimens with various sizes and aspect ratio. The proposed equation is written in terms of imperial unit: $\frac{P}{P_6} = 0.56 + \frac{0.697}{\frac{V}{6hd}+\frac{h}{d}}$, for which it is rewritten here with constants to be fitted and in metric system:

$$\frac{f'_{cy}(V, d, \frac{h}{d})}{f'_c} = a + \frac{b}{\frac{V}{152.4hd} + \frac{h}{d}} \tag{5}$$

Building on the Bažant SEL [1] that considers the energy balance at crack propagation in concrete, Kim & Yi et. al. [59] proposed the following expression in Eq. 6 from statistical analysis. However, this equation has a limitation since it applies only to specimens with an aspect ratio greater than 1. As when $h/d$ falls less than 1, the strength decreases with reducing aspect ratio, which is contrary to reality. From a mathematical point of view, when the aspect ratio falls less than 1, the term in the square root bears also the risk of becoming negative. This limitation and the empirical value of the 50 in the equation make it an insufficient mathematical tool for describing general size effect in compression.

$$\frac{f'_{cy}}{f'_c} = \frac{a}{\sqrt{1 + (h - d)/50}} + b \tag{6}$$

Table 9: Size effect data fit with known $f_c'$

| Model | Concrete & Shape | | $a$ | $b$ | $R^2$ |
|---|---|---|---|---|---|
| Neville | C50 Prism | | 0.877 | 1.69 | 0.686 |
| | C50 Cylinder | | 0.931 | 1.09 | 0.669 |
| | UHPC Prism | | 0.864 | 0.786 | 0.875 |
| | UHPC Cylinder | | 0.895 | 0.630 | 0.891 |
| Kim&Yi | C50 Prism | | 0.643 | 0.960 | 0.899 |
| | C50 Cylinder | | 0.483 | 0.981 | 0.945 |
| | UHPC Prism | | 0.530 | 0.825 | 0.910 |
| | UHPC Cylinder | | 0.457 | 0.860 | 0.913 |
| Model | Concrete & Shape | $d_0$ | $p$ | $q$ | $R^2$ |
| ComSEL3D | C50 Prism | 2.77 | 1.332 | 0.270 | 0.987 |
| | C50 Cylinder | 1.14 | 1.289 | 0.157 | 0.995 |
| | UHPC Prism | 0.68 | 1.695 | 0.133 | 0.993 |
| | UHPC Cylinder | 0.68 | 1.648 | 0.154 | 0.998 |

The two formulas by Neville and Kim&Yi are used to fit the compressive test data of various sizes for C50 and the UHPC. For the data fitting, the value of $f_c'$ is taken to be equal to 50 MPa and 220 MPa respectively for the two concrete grades. The reason lies in the concrete itself: both concretes are classified with the aforementioned strengths as confirmed by tests under compression with low friction settings. Moreover, for high aspect ratio equals h/d = 4, both concretes show nearly no size effect and thus the compressive strength should be close to the asymptotic value. The data fitting results including the coefficients and the correlation are shown in Table 9. The Neville equation is found to be inefficient as the correlation $R^2$ values are below 0.9, as similarly found in [61]. Although the Kim&Yi formula is better in the data fit with higher $R^2$ values, it has the limitation on the exclusion of small aspect ratio, i.e. $H/D < 1$.

Due to the inefficiency and limitations of available size effect laws, the authors want to propose in this paper a new formula to describe and predict the size effect of concrete under compressive loading. The

statistical size effect is always present, but its effect is very small when the fracture size effect is dominant as in compression failure. The statistical size effect due to random strength becomes important only for large structures for which the failure occurs at crack initiation from a smooth surface [2, 17]. However, this is out of the scope of this study. To take into account not just the diameter as a single variable but also the height or equivalently the aspect ratio, $s$, the $D_0$ in Eq.4 is found to have a relation with the aspect ratio, $D_0 \propto s^p$, and the formula is expanded as

$$\frac{\sigma_N}{f_c^\infty} = \left(\frac{1}{s}\right)^p \left(\frac{d_0}{d}\right)^q + 1 \tag{7}$$

where $d_0$, $p$ and $q$ are dimensional constants. As this size effect law is based on ComSEL and considers all three dimensions of the structure, here it is termed ComSEL3D. By imposing $f_c^\infty$ equals 50 MPa and 220 MPa respectively for the C50 and UHPC, the proposed ComSEL3D formula is used for data fitting. In comparison with Neville and Kim&Yi formulas, the results are presented in Table 9. The size effect analysis plots of strength vs. diameter, strength vs. height, strength vs. volume, strength vs. aspect ratio, and the fitted data sets are included in Fig. 28-31. In subfigures (a), the CSEL formula is used to fit the results for individual aspect ratio. In general, CSEL gives quite good correlation of fits for the individual aspect ratio, however it cannot be used to fit data with variable aspect ratio. As shown in subfigures (d), the ComSEL3D gives correlation $R^2$ values above 0.99 for both concretes and both shapes, which outperforms the aforementioned size effect formulas available in the literature. This makes ComSEL3D the most capable mathematical tool to describe and predict the size effect for concrete under compression.

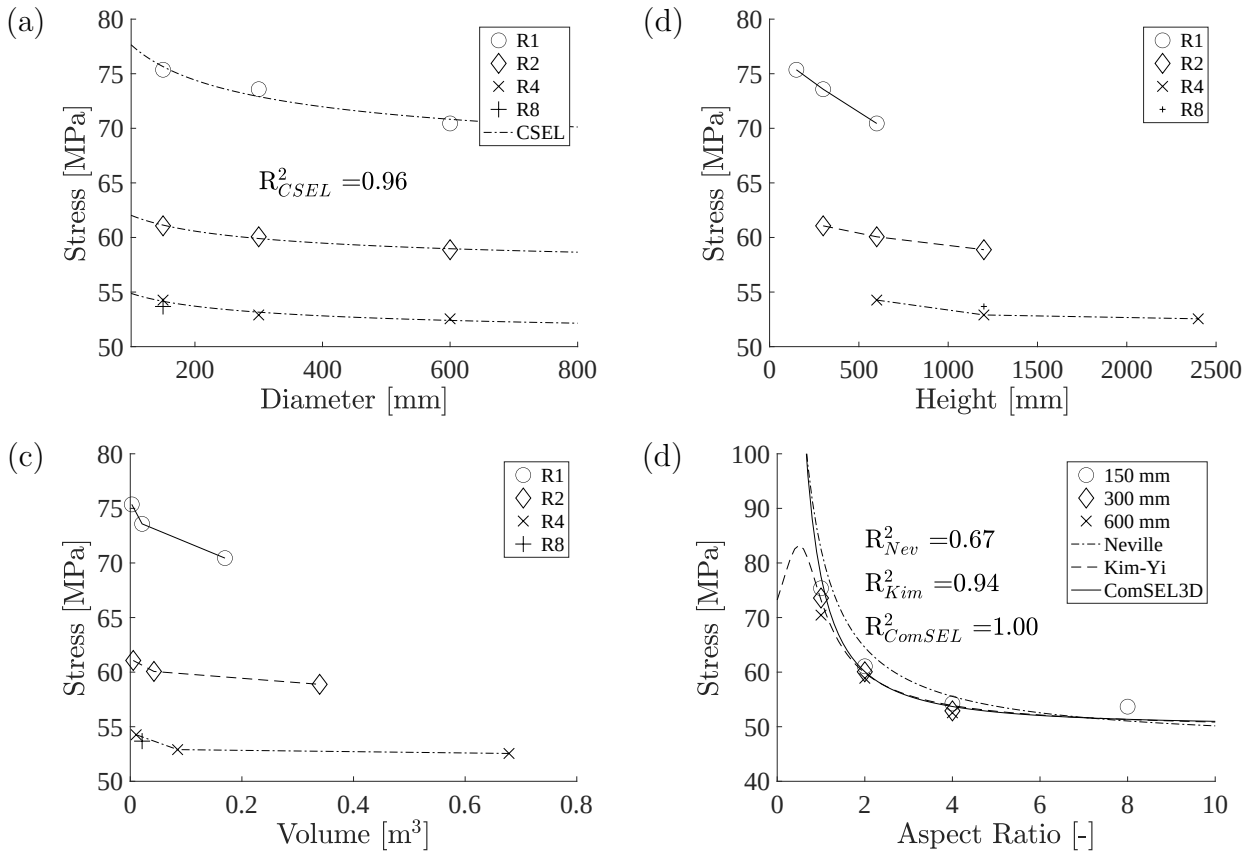


Figure 28: Compressive strength of C50 cylinders as function of the specimen diameter (a); height (b); volume (c); aspect ratio (d).

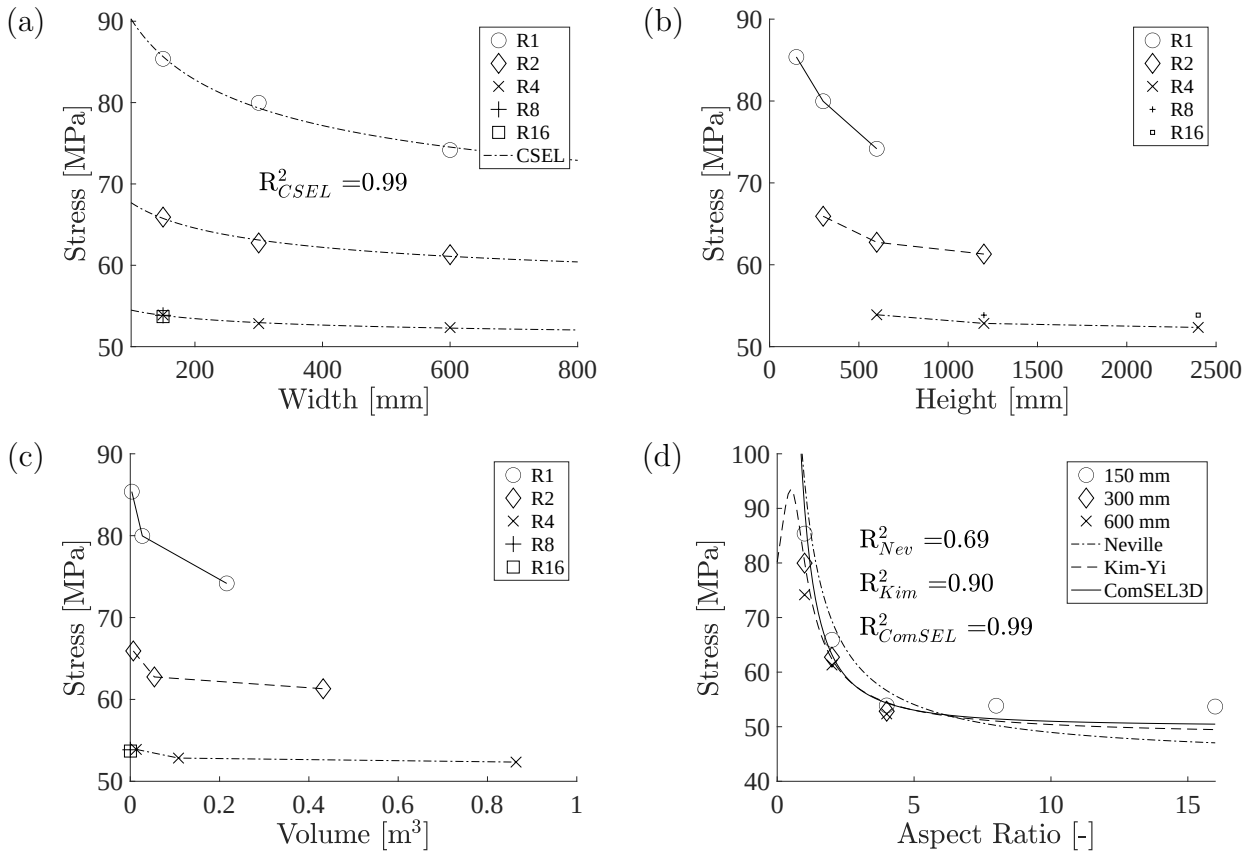


Figure 29: Compressive strength of C50 prims as function of the specimen diameter (a); height (b); volume (c); aspect ratio (d).

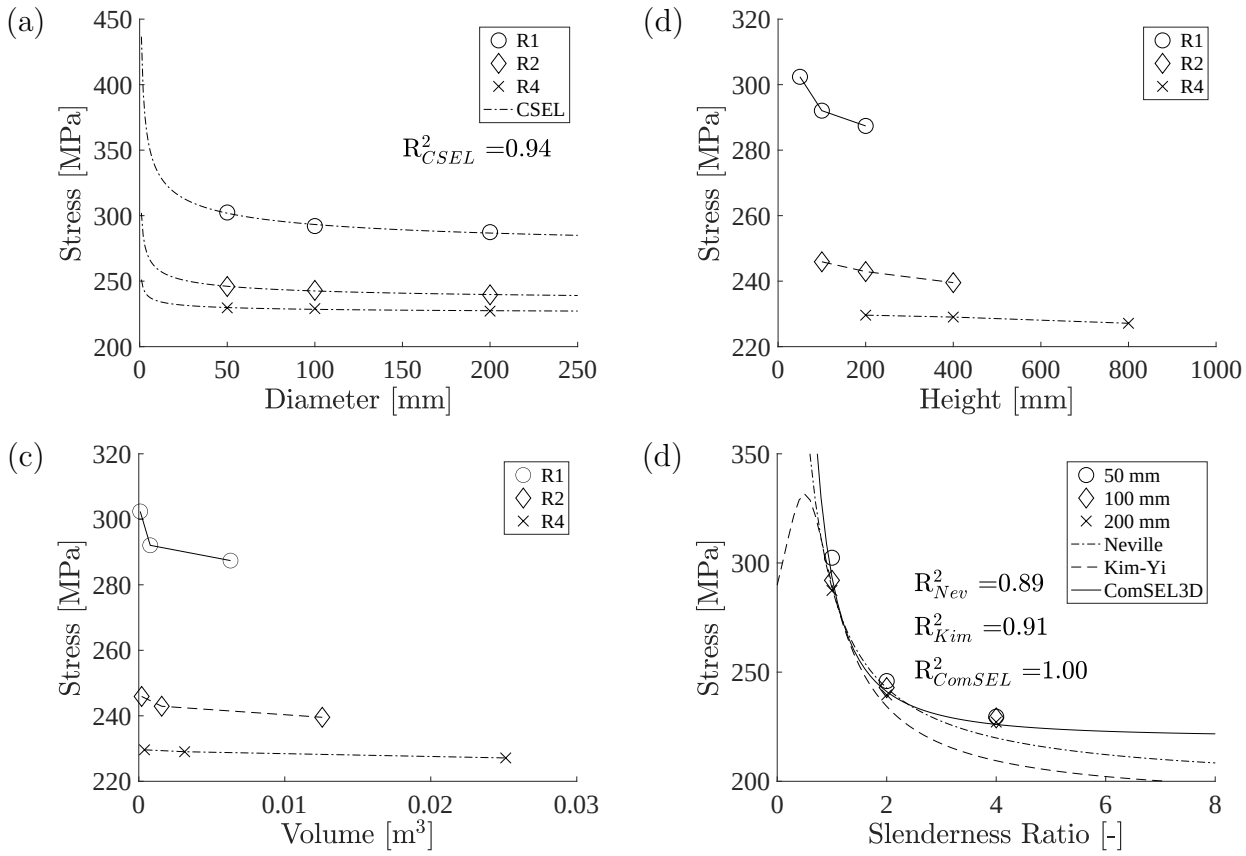


Figure 30: Compressive strength of UHPC cylinders as function of the specimen diameter (a); height (b); volume (c); aspect ratio (d).

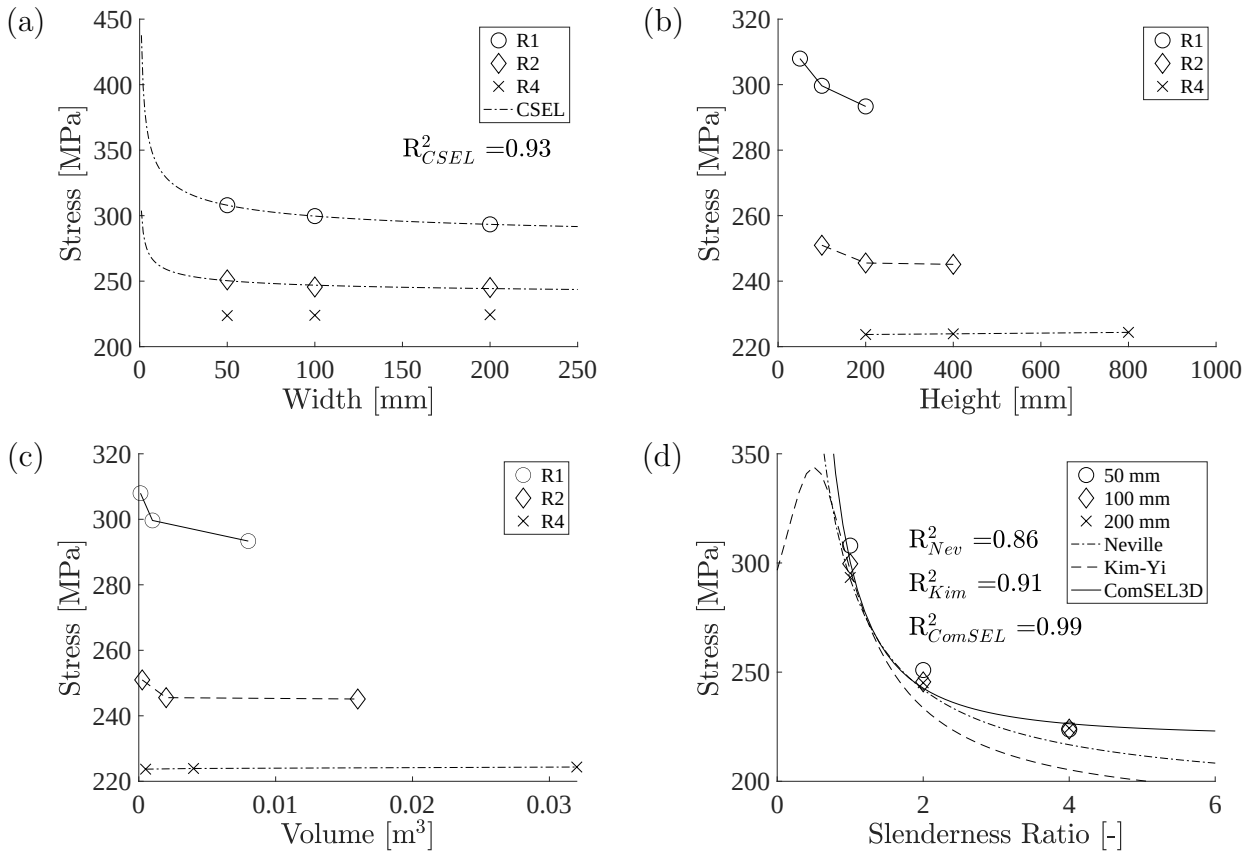


Figure 31: Compressive strength of UHPC prisms as function of the specimen diameter (a); height (b); volume (c); aspect ratio (d).

For the sake of simplicity, the term $D_0$ can be kept which includes both the length scale and the strength contributions, $D_0 = d_0 f_c^{\infty}$, where $d_0$ is a length scale parameter. The coefficient $p$ is found to be consistent for all data sets of concrete grades and specimen shapes $p = 3/2$. Similarly the value of coefficient $q$ can be fairly set to $q = 1/5$. The size effect law for concrete under compression ComSEL3D is rewritten to also account for the scenario when $f_c^{\infty}$ is not known. The equation describes the deterministic size effect for the investigated C50 and UHPC and is termed ComSEL3D$^{\star}$:

$$\sigma_N = \left[ \left( \frac{1}{s} \right)^{3/2} \left( \frac{d_0}{d} \right)^{1/5} + 1 \right] f_c^{\infty} \tag{8}$$

The deterministic size effect formula ComSEL3D$^{\star}$ is used to fit the compressive strength data for C50 and UHPC. For comparison, the equation of Kim&Yi [59] with fixed coefficients $f'_{cy} = f'_c(\frac{0.4}{\sqrt{1+(h-d)/50}} + 0.8)$ is used also for data fitting, mainly to compare the value of $f_c^{\infty}$ and $f'_c$ which are equivalent and represent

the nominal strength of infinitely large structures or the non-changing part of the strength.

The data-fitting results using ComSEL3D$^\star$ and in comparison Kim&Yi are shown in Table 10. The ComSEL3D$^\star$ gives correlation $R^2$ values above 0.97 up to 1.00 for both concretes and shapes with the average $R^2 = 0.988$. Moreover, the acquired $f_c^\infty$ value from data fitting by ComSEL3D$^\star$ is in general lower and closer to the nominal strength of the corresponding concrete and shape when compared to that of Kim&Yi. The difference between the ComSEL3D$^\star$ fitted $f_c^\infty$ and the nominal strength of the concretes is up to about 2%, which is normally less than the variation in the experimentally tested compressive strength.

Table 10: Size effect data fit with unknown $f_c^\infty$

| | Model | $d_0$ | $f_c^\infty$ | $R^2$ |
|---|---|---|---|---|
| C50 Prism | ComSEL3D$^\star$ | 21.0 | 51 | 0.977 |
| | Kim&Yi | | 65 | 0.864 |
| C50 Cylinder | ComSEL3D$^\star$ | 4.32 | 51 | 0.990 |
| | Kim&Yi | | 61 | 0.945 |
| UHPC Prism | ComSEL3D$^\star$ | 0.93 | 215 | 0.992 |
| | Kim&Yi | | 243 | 0.893 |
| UHPC Cylinder | ComSEL3D$^\star$ | 0.47 | 218 | 0.995 |
| | Kim&Yi | | 240 | 0.911 |

## 5 Shape Effect

Looking into the shape effect by comparing the compressive strengths of prism and that of cylinder, it is found that the difference may be caused by confinement due to friction as well. Calculated and shown in Table 11 is the ratio of compressive strength of prism divided by that of cylinder under high friction condition. The difference is the most prone with low aspect ratio and diminishes with rising aspect ratio. The normal strength concrete exhibits higher difference between prism and cylinder, with the highest value of 13% for the smallest size and lowest aspect ratio, whereas it is less than 3% for UHPC. For aspect ratio equal to 4, the difference in prism and cylinder for both concretes is below about 2%, hinting that the

shape effect, similar to size effect, plays a role only when confinement by loading platens is present. This is supported by the fact that there is nearly no difference in strengths of various sizes under low friction between the two shapes and that the strengths of highly slender specimens have almost the same strengths as those under low friction. In other words, for both scenarios either under low friction or with high aspect ratio, the specimens do not feel the confinement at the ends and consequently display neither size effect nor shape effect.

Going back to the size effect data fitting by ComSEL3D$^\star$ as shown in Table 10, the main difference due to shape effect lies in the fitted value of $d_0$. By dividing $d_0$ of prism by $d_0$ of cylinder, the ratio is computed to be 1.37 for C50 and 1.15 for UHPC. For the cross section of cylinder and prism, the ratio is $4/\pi$=1.27 for both the area and circumference. This is supposedly already taken into account by the stress calculation. In comparison, C50 displays much higher difference in strength by shape than UHPC. This may be explained by the high resistance of stronger concrete to the confinement effect due to friction. Moreover, the aggregate size of the UHPC is much smaller than that of C50. An interesting comparison is to put the $d_0$ shape ratio and the sizes difference into one picture. The $d_0$ ratio difference by shape of 37% for C50 divide by 15% for UHPC equals 2.5. Considering that the C50 specimens are 3 times larger than that of the UHPC and the largest aggregate size of C50 is 8 times larger than that of UHPC, the relative difference is about 2.6. This close comparison may shed some light on the mechanism of size/shape effect, that concrete with larger aggregates and hence usually lower strength are more crude against end confinement and the size/shape effect may be proportional to that resistance.

Table 11: Shape ratio of prism to cylinder compressive strengths

| C50 | d=150 | d=300 | d=600 | Average |
|---|---|---|---|---|
| S=1 | 1.133 | 1.087 | 1.053 | 1.091 |
| S=2 | 1.080 | 1.045 | 1.041 | 1.055 |
| S=4 | 0.993 | 0.999 | 0.996 | 0.996 |
| UHPC | d=50 | d=100 | d=200 | Average |
| S=1 | 1.018 | 1.026 | 1.021 | 1.022 |
| S=2 | 1.021 | 1.011 | 1.023 | 1.018 |
| S=4 | 0.974 | 0.978 | 0.988 | 0.980 |

## 6 Comparison with experimental results in literature

To determine the effective trend of the size effect in compression, a large size scale must be considered. However, only few experimental investigations span over large scale ranges, although a large amount of experimental researches on uniaxial compressive strength have been performed over the years. In this section the available experimental investigations from literature carried out on cylindrical and prismatic specimens with different aspect ratios, $H/D$, are considered. In particular, the following experimental campaigns on cylinders are taken into account: Blanks and McNamara [13] with $H/D = 2$, Burtscher and Kollegger [23] with $H/D = 4$, Muciaccia et al. [17] with $H/D = 2$ and $H/D = 4$, Sener [32] with $H/D = 2$, Asadollahi et. al. [33] with $H/D = 2$. In addition, the following experimental tests are considered: on prisms by Jishan and Xixi [18] with $H/D = 1$ and $H/D = 3$, on cylinders and prisms by Sim et al. [34] with $H/D = 1$ and $H/D = 2$, on cylinders with $H/D = 2$ and cubes by Del Viso et. al. [35], and on cylinders with $H/D = 2$ and prisms with $H/D = 1$ and $H/D = 2$ by Yi et. al. [36].

Considering all the above mentioned experimental data, the best fitting with the size effect law ComSEL3D, is here repeated using the Levenberg-Marquardt nonlinear optimization. The nominal strength of each series is normalized with respect to the conventional compressive strength, i.e. the compressive strength of the cylinder with 150 mm of diameter and height of 300 mm. When this geometry is not available the strength of the closest size is adopted for the conventional compressive strength. As it can be observed in Figure 32, in which the normalized nominal strengths are plotted for different aspect ratios, the size effect exhibited by the experimental data presents a much stronger reduction of the compressive strength with increasing size than the predictions of the mesoscale model. The optimized value of the parameters are reported in the Table 12 and the corresponding fitted size effect curves are plotted in the Figure 32 in semi-logarithmic scales.

| ComSEL | ComSEL3D | ComSEL3D* |
|---|---|---|
| $f_c^\infty = 0.599$ | $f_c^\infty$=0.58 | $f_c^\infty$=0.88 |
| $D_0 = 16.24$ mm | $d_0$ =101.5 mm | $d_0$ =0.373 mm |
| | $p$ =0.29 | $p$ =3/2=1.5 |
| | $q$ =0.36 | $q$ =1/5=0.2 |
| $R^2 = 0.558$ | $R^2 = 0.674$ | $R^2 = 0.3084$ |

Table 12: Parameters and coefficient of determination, $R^2$, of the different size effect laws.

All the experimental data present a similar trend and the size effect laws, ComSEL and ComSEL3D, are very close especially for aspect ratio equal to 1 and 2. The ComSEL3D gives the best overall description of the experimental data analyzed with a $R^2 = 0.674$. This proves that ComSEL3D is the best formula so far in the available literature to describe the size effect of concrete under compression. The formula ComSEL3D can be used for any type of concrete for compressive size effect for data fitting and prediction.

However, the ComSEL3D law with the exponential coefficients, $p$ and $q$, fitted on the results of the C50 and UHPC numerical analysis, which is here termed as ComSEL3D$^*$, presents a bad fitting of the experimental data from literature on the size effect in compression with $R^2 = 0.3084$, see also the red line in Figure 32. This means that the deterministic size effect in compression predicted by the mesoscale LDPM model does not fully agree with the experimental data from literature, on the contrary of the tensile size effect which is very well captured by the model, for instance see [50]. The possible causes of that may be:

- the LDPM doesn't consider statistical effects, which may play an important contribution for larger sizes and for aspect ratio greater than 2.
- experimental data may present larger size effect due to non-uniform drying, imperfect geometry of the specimens, different amount of friction between specimen and loading platens, wall effect.

On the other hand, we cannot use the mesoscale LDPM to model directly the experimental data on compressive size effect because not enough data are available to calibrate properly the model as discussed previously.

All the simulations so far were performed on a deterministic basis. The randomness of concrete mechanical properties is partially due to aggregate size distribution and the efficiency of LDPM to capture this aspect has already been proven. However, in concrete, the inconstancy of material parameters at different locations has also a tremendous effect on the fluctuation of the mechanical behavior. In order to fully capture the randomness of mechanical properties in concrete, LDPM should be extended to take into account the probabilistic spatial distribution of the LDPM mesoscale parameters through the incorporation of a random field model [65]. The sources of such variations are numerous, among others the effect of concrete structure geometry, the difference in relative humidity, as well as the local curing in concrete. In any case, the investigation on these issues is left for future studies.

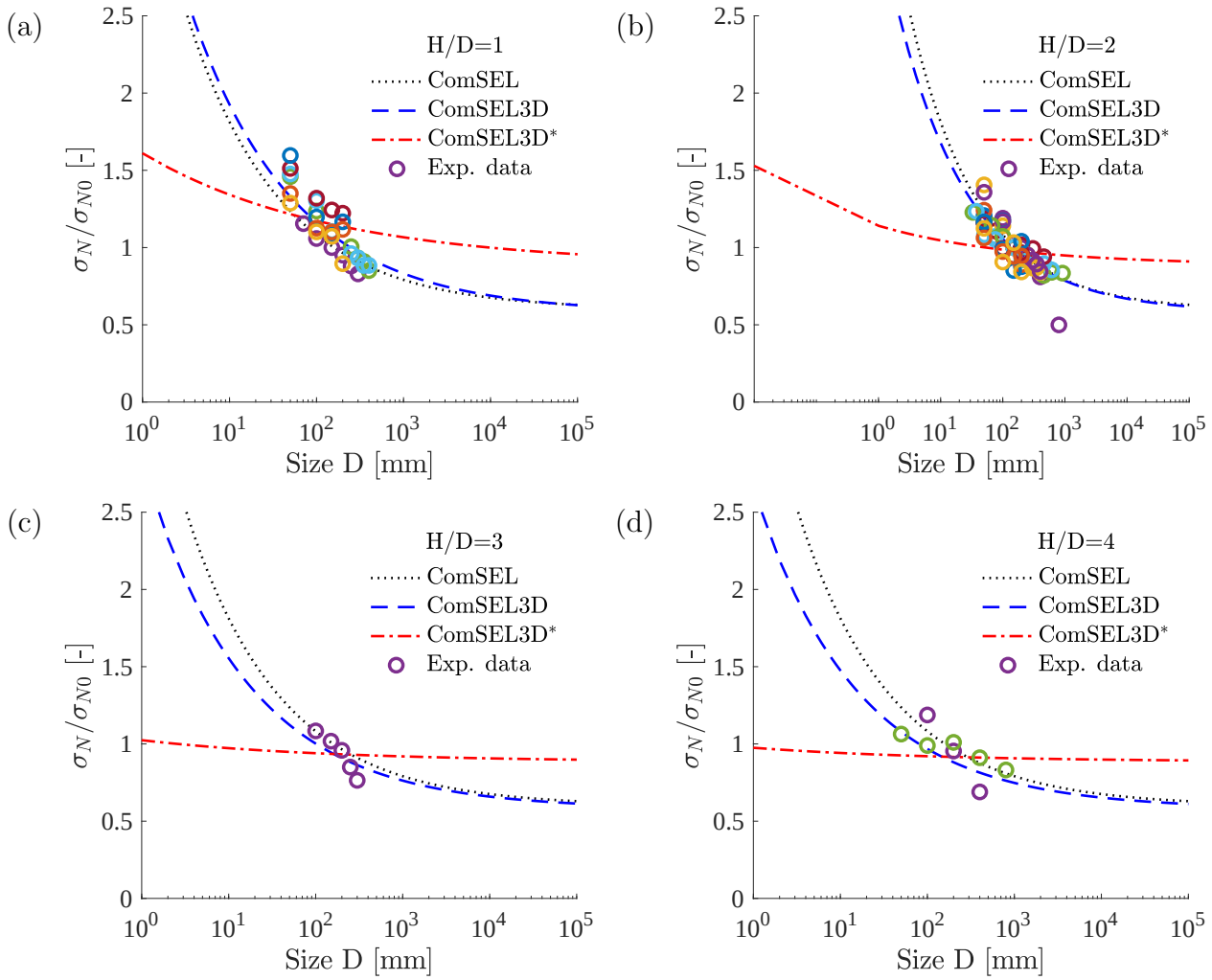


Figure 32: Size effect plots in semi-logarithmic scale for different specimen aspect ratios: comparison between experimental data (circles) and size effect curves (lines).

## 7 Conclusions

In conclusion, the Lattice Discrete Particle Model (LDPM) can be utilized to simulate the deterministic size effect in compression of various concretes. With the minimum amount of experimental tests of compressive and tensile loading with one size of specimen, the LDPM mesoscale parameters can be calibrated and the strengths of other sizes can be predicted using the same data-set. The scatter of simulated strengths is well considered by running multiple simulations with different spatial distribution of aggregates, just as in reality. The post-peak behavior can as well be obtained through LDPM, which indicates the ductility/brittleness of the tested material under compressive loading. However, the LDPM compressive size effect results do not fully agree with the available experimental results in the literature, especially for

aspect ratio grater than 2, partially due to lack of a fully statistical setup in the model and imperfections in setting up experiments. This leaves room for future further studies on the enhancement of LDPM with the randomness distribution of the mechanical properties.

It is found from the studied tests that deterministic size effect in compression is only exhibited with high friction conditions. In other words, it is confirmed that the deterministic size effect in compression is mainly caused by end confinement. Moreover, the magnitude of size effect in compression diminishes with rising aspect ratio. From a practical point of view, the corresponding researchers and practitioners should be aware of the size effect in compression with high friction loading. It is recommended to either apply low friction, e.g. with teflon sheets, or use slender specimens with aspect ratio larger than 4 to minimize the effect from end confinement on concrete failure.

Furthermore, the proposed compressive size effect law ComSEL3D is found to be able to perfectly describe the deterministic size effect in compression of various sizes and aspect ratio. The fitted data using ComSEL3D gives correlation $R^2$ value of more than 0.99 for the studied normal strength and ultra high strength concrete (UHPC) and for both cylinders and prisms. The formula also outperforms the other equations available in the literature in matching the experimental results of concrete under compression by various researchers. This proves for the ComSEL3D to be a useful mathematical tool to predict the size effect in compression of concretes.

## References


[1] Bažant, Z. P., Size Effect in Blunt Fracture: Concrete, Rock, Metal, Journal of Engineering Mechanics, ASCE, 110(4), 1984, 518-535.

[2] Z.P. Bažant, J. Planas, Fracture and Size Effect in Concrete and Other Quasibrittle Materials, CRC Press, Boca Raton, Florida, 1998.

[3] Z. P. Bažant, Q. Yu. Universal size effect law and effect of crack depth on quasi-brittle structure strength Journal of Engineering Mechanics, ASCE, Feb, 2009.

[4] Z.P. Bažant. Size effect in tensile and compression fracture of concrete structures: computational modeling and design. Fracture Mechanics of Concrete Structures Proceedings FRAMCOS-3, 1998.

[5] ACI, American Concrete Institute, Committee 318. ACI CODE-318-19: Building Code Requirements for Structural Concrete and Commentary. 2019.

[6] van Mier, J.G.M., 1986. Multiaxial strain-softening of concrete. Part I: Fracture. Materials and Structures 19, 179–190.

[7] van Vliet, M.R.A., van Mier, J.G.M., 1995. Softening behavior of concrete under uniaxial compression. AEDIFICATIO Publishers, D-79194 Freiburg. Folker h. Wittman edition. pp. 383–396.

[8] Cedolin, L., Cusatis, G., 2008. Identification of concrete fracture parameters through size effect experiments. Cement and Concrete Composites 30, 788 – 797.

[9] Di Luzio, G., Biolzi, L., 2013. Assessing the residual fracture properties of thermally damaged high strength concrete. Mechanics of Materials 64, 27 – 43.

[10] Di Luzio, G., Muciaccia, G., Biolzi, L., 2010. Size effect in thermally damaged concrete. International Journal of Damage Mechanics 19, 631–656.

[11] Hoover, C.G., Bažant, Z.P., Vorel, J., Wendner, R., Hubler, M.H., 2013. Comprehensive concrete fracture tests: Description and results. Engineering Fracture Mechanics 114, 92–103.

[12] Belgin, C., Sener, S., 2008. Size effect on failure of over-reinforced concrete beams. Engineering Fracture Mechanics 75, 2308–2319.

[13] Blanks, R.F., McNamara, C.C., 1935. Mass concrete tests in 1arge cylinders. Journal of American Concrete Institute 31, 280–303.

[14] Gonnermann, H.F., 1925. Effect of size and shape of test specimen on compressive strength of concrete. Proceedings ASTM 25, 237–250.

[15] Abdalla Talaat and Abdelrhman Emad and Ahmed Tarek and Mohamed Masbouba and Ashraf Essam and Mohamed Kohail, Factors affecting the results of concrete compression testing: A review, Ain Shams Engineering Journal, 12(1):205-221, 2021.

[16] Jansen, D., Shah, S., 1997. Effect of length on compressive strain softening of concrete. Journal of Engineering Mechanics, ASCE 123, 25–35.

[17] G. Muciaccia, G. Rosati, G. Di Luzio. Compressive failure and size effect in plain concrete cylindrical specimens. Construction and Building Materials 137 (2017) 185–194.

[18] Jishan, X., Xixi, H., 1990. Size effect on the strength of a concrete member. Engineering Fracture Mechanics 35, 687–695.

[19] Bažant, Z.P., Kwon, Y.W., 1994. Failure of slender and stocky reinforced concrete columns: tests of size effect. Materials and Structures 27, 79.

[20] Hollingworth, S., 1998. Structural and mechanical properties of high strength concrete. Civil Engineering PhD Thesis. Division of Civil Engineering, University of Wales. Cardiff, Wales.

[21] Sener, S., Barr, B., Abusiaf, H., 1999. Size effect tests in unreinforced concrete columns. Magazine of Concrete Research 51, 3–11.

[22] Němeček, J., 2000. Modelling of compressive softening of concrete. Civil Engineering PhD Thesis. Department of Structural Mechanics, CTU Prag. Prag, Czech Republic.

[23] Burtscher, S., Kollegger, J., 2004. Size effect of sandstone and concrete., in: Li, V., Willam, K., Leung, C., Billington, S. (Eds.), 5th International Conference on Fracture Mechanics of Concrete and Concrete Structures - FraMCoS-5.

[24] Hillerborg A., Modéer M., Petersson P.-E., Analysis of crack formation and crack growth in concrete by means of fracture mechanics and finite elements, Cement and Concrete Research, 6(6):773-781, 1976.

[25] G. Di Luzio and Z. P. Bažant, Spectral analysis of localization in nonlocal and over-nonlocal materials with softening plasticity or damage, International Journal of Solids and Structures, 42(23):60716100, 2005.

[26] G. Di Luzio, A symmetric over-nonlocal microplane model M4 for fracture in concrete, International Journal of Solids and Structures, 44(13):44184441, 2007.

[27] Vorel J., Marcon M., Cusatis G., Caner F., Di Luzio G., Wan-Wendner R., A comparison of the state-of-the-art models for constitutive modelling of concrete, Computer and Structures, 244:106426, 2021.

[28] Oliver J, Huespe AE, Pulido MDG, Chaves E., From continuum mechanics to fracture mechanics: the strong discontinuity approach, Engineering Fracture Mechanics, 69(2):113136, 2002.

[29] Rabczuk T, Zi G, Bordas S, Nguyen-Xuan H., A geometrically non-linear three-dimensional cohesive crack method for reinforced concrete structures, Engineering Fracture Mechanics, 75:47404758, 2008.

[30] Sukumar N, Dolbow JE, Moës N., Extended finite element method in computational fracture mechanics: a retrospective examination, International Journal of Fracture, 196:189206, 2015.

[31] Ožbolt, J., Eligehausen, R., 1995. Size effect in concrete and reinforced concrete structures., in: Wittmann, F.H. (Ed.), 2th International Conference on Fracture Mechanics of Concrete and Concrete Structures - FraMCoS-2, AEDIFICATIO Publishers, D-79104 Freiburg. pp. 665–674.

[32] Sener S., Size effect tests of high strength concrete, Journal of Materials in Civil Engineering ASCE, 9(1):46–8, 1997.

[33] S. Asadollahi and A. Saeedian and M. Dehestani and F. Zahedi, Improved compressive fracture models for self-consolidating concrete (SCC), Construction and Building Materials, 123:473–480, 2016.

[34] Jae-Il Sim and Keun-Hyeok Yang and Heung-Yeoul Kim and Byong-Jeong Choi, Size and shape effects on compressive strength of lightweight concrete, Construction and Building Materials, 38:854–864, 2013.

[35] J.R. del Viso and J.R. Carmona and G. Ruiz, Shape and size effects on the compressive strength of high-strength concrete, Cement and Concrete Research, 38(3):386–395, 2008.

[36] Yi, Seong-Tae and Yang, Eun-Ik and Choi, Joong-Cheol, Effect of specimen sizes, specimen shapes, and placement directions on compressive strength of concrete, Nuclear Engineering and Design, 236(2):115-127, 2006.

[37] G. Cusatis, Z.P. Bažant, and L. Cedolin, Confinement-shear lattice model for concrete damage in tension and compression. I. theory, Journal of Engineering Mechanics, ASCE, 129(12):1439–1448, 2003.

[38] G. Cusatis, Z.P. Bažant, and L. Cedolin, Confinement-shear lattice model for concrete damage in tension and compression. II. computation and validation, Journal of Engineering Mechanics, ASCE, 129(12):1449-1458, 2003.

[39] G. Cusatis, Z.P. Bažant, and L. Cedolin, Confinement-shear lattice CSL model for fracture propagation in concrete, Computer Methods in Applied Mechanics and Engineering, 195 (2006) 7154-7171.

[40] G. Cusatis, D. Pelessone, and A. Mencarelli. Lattice discrete particle model (LDPM) for failure behavior of concrete. I: Theory, Cement Concrete Composites, 33(9), 881-890, (2011).

[41] G. Cusatis, D. Pelessone, and A. Mencarelli. Lattice discrete particle model (LDPM) for failure behavior of concrete. II: Calibration and validation, Cement Concrete Composites, 33(9), 891-905, (2011).

[42] L. Wan, R. Wendner, B. Liang, G. Cusatis. Analysis of the Behavior of Ultra-High-Performance-Concrete at Early Age, Cement and Concrete Composites, 2016. doi: 10.1016/j.cemconcomp.2016.08.005

[43] L. Wan, R. Wendner, G. Cusatis. Behavior of Ultra-High-Performance Concrete at Early age: Experiments and Simulations. First International Interactive Symposium on UHPC, 2016. doi: 10.21838/uhpc.2016.7

[44] L. Wan. Experimental and Computational Analysis of the Behavior of Ultra High Performance Concrete, Prestressed Concrete, and Waterless Martian Concrete at Early Age and Beyond, Northwestern University, 2015.

[45] L. Wan, R. Wendner, G. Cusatis. A Novel Material for In Situ Construction on Mars: Experiments and Numerical Simulations. Construction and Building Materials, 120, 222-231, 2016, doi:10.1016/j.conbuildmat.2016.05.046

[46] L. Wan, R. Wendner, G. Cusatis. A Hygro-Thermo-Chemo Mechanical Model for the Simulation of Early Age Behavior of Ultra-High-Performance Concrete, CONCREEP 10: pp. 166-175, Vienna, Austria, Sep 2015, doi: 10.1061/9780784479346.020.

[47] G. Boumakis, M. Marcon, L. Wan, R. Wendner. Creep and Shrinkage in Fastening Systems, CONCREEP 10: pp. 657-666, 2015, doi: 10.1061/9780784479346.079.

[48] R. Wendner, K. Nincevic, I. Boumakis, L. Wan. Age-Dependent Lattice Discrete Particle Model for Quasi-Static Simulations. Key Engineering Materials, 1662-9795, Vol. 711, pp 1090-1097, 2016, doi:10.4028/www.scientific.net/KEM.711.1090

[49] L Wan-Wendner, J Vorel, A Strauss, G Cusatis, R Wan-Wendner. Discrete modeling of reinforced and prestressed concrete beams under shear loads IABSE Symposium Report 109 (40), 1766-1773, 2017.

[50] L. Wan-Wendner, R. Wan-Wendner, G. Cusatis. Age-dependent size effect and fracture characteristics of ultra-high performance concrete. Cement and Concrete Composites, 2018. doi: 10.1016/j.cemconcomp.2017.09.010

[51] Slowik O., Novak D., Krug B., Strauss A. Shear failure of prestressed concrete T-shaped girders: Experiment and nonlinear modeling. IABSE Conference - Structural Engineering: Providing Solutions to Global Challenges, 2015.

[52] Nguyen, Hoang, Pathirage, M., Cusatis, G., and Bažant, Z.P. Gap test of crack-parallel stress effect on quasi-brittle fracture and its consequences. Journal of Applied Mechanics, ASME 87, 2020, 071012-1-11.

[53] E. A. Schauffert, and G. Cusatis. Lattice discrete particle model for fiber-reinforced concrete. I: theory, Journal of Engineering Mechanics, ASCE, 2012, 826-833.

[54] E. A. Schauffert, G. Cusatis, D. Pelessone, J. L. O'Daniel, and J. T. Baylot. Lattice discrete particle model for fiber-reinforced concrete. II: tensile fracture and multiaxial loading behavior, Journal of Engineering Mechanics, ASCE, 2012, 834-841.

[55] J. Smith, G. Cusatis, D. Pelessone, E. Landis, J. O'Daniel, J. Baylot. Discrete modelling of ultra-high-performance concrete with application to projectile penetration, International Journal of Impact Engineering 65, 2014, 13-32.

[56] Bažant, Z.P., and Ožbolt, J. Compression failure of quasi-brittle material: Nonlocal microplane model Journal of Engineering Mechanics, ASCE, 118(3), 540–556, (1992).

[57] Cusatis, G. , Bažant, Z.P., 2006. Size effect on compression fracture of concrete with or without V-notches: a numerical mesomechanical study., in: G. Meschke, R. de Borst, H. Mang, N. Bicanic (Eds.), Conference on Computational Modelling of Concrete Structures - EURO-C 2006, Taylor & Francis, 71-83

[58] A.M. Neville. A general relation for strength of concrete specimens of different shape and size. Journal of the American Concrete Institute, 1966;63(10):1095-110.

[59] Kim JK, Yi ST, Park CK, Eo SH. Size effect on compressive strength of plain and spirally reinforced concrete cylinders. ACI Structural Journal, 1999;96(1):88-94.

[60] Kim JK, Yi ST. Application of size effect to compressive strength of concrete members. Sadhana 2002;27(4):467-84.

[61] M. Dehestani, I.M. Nikbin, S. Asadollahi. Effects of specimen shape and size on the compressive strength of self-consolidating concrete (SCC). Construction and building materials, 66 (2014) 685-691.

[62] van Mier, J.G.M., 1998. Failure of concrete under uniaxial compression: an overview., in: Mihashi, H., Rokugo, K. (Eds.), 3th International Conference on Fracture Mechanics of Concrete and Concrete Structures - FraMCoS-3, AEDIFICATIO Publishers, D-79104 Freiburg. pp. 1169–1182.

[63] Bažant, Z. P. and Xiang, Y., Size effect in compression fracture: Splitting crack band propagation. Journal of Engineering Mechanics, ASCE, 123(2), 1997, 162-172.

[64] Alnaggar, M., Pelessone, D., Cusatis, G., Lattice Discrete Particle Modeling of Reinforced Concrete Flexural Behavior. Journal of Structural Engineering, ASCE, 145(1), 2019, 04018231.

[65] M. Pathirage, Multi-scale multi-physics modeling of alkali-silica reaction in concrete: experimental investigation and numerical prediction. PhD Thesis, Northwestern University, June 2020.

[66] W. G. Noid, Jhih-Wei Chu, Gary S. Ayton, Vinod Krishna, Sergei Izvekov, Gregory A. Voth, Avisek Das, and Hans C. Andersen, The multiscale coarse-graining method. I. A rigorous bridge between atomistic and coarse-grained models. J. Chem. Phys., 128, 2008, 244114.

[67] Erol Lale, Roozbeh Rezakhani, Mohammed Alnaggar, Gianluca Cusatis, Homogenization coarse graining (HCG) of the lattice discrete particle model (LDPM) for the analysis of reinforced concrete structures. Engineering Fracture Mechanics, 197, 2018, 259-277.

[68] Abdellatef M., Alnaggar M., Energy-Based Coarse Graining of the Lattice-Discrete Particle Model. Journal of Engineering Mechanics, 146(5), 2022, 04020026.

[69] Vonk RA., Softening of concrete loaded in compression. PhD thesis, Eindhoven University of Technology; 1992.